

NRL Report 8321

00
01
02
03
04
05
06
07
08
09
10
11
12

A Global Ionospheric Model

JOE THOMASON AND GLENN SKAGGS

*Radar Techniques Branch
Radar Division*

JOHN LLOYD

*Institute for Telecommunication Sciences
Department of Commerce
Boulder, Colorado*

August 20, 1979



NAVAL RESEARCH LABORATORY
Washington, D.C.

Approved for public release; distribution unlimited.

REPORT DOCUMENTATION PAGE		READ INSTRUCTIONS BEFORE COMPLETING FORM
1. REPORT NUMBER NRL Report 8321	2. GOVT ACCESSION NO.	3. RECIPIENT'S CATALOG NUMBER
4. TITLE (and Subtitle) A GLOBAL IONOSPHERIC MODEL	5. TYPE OF REPORT & PERIOD COVERED Interim report on a continuing NRL problem	
	6. PERFORMING ORG. REPORT NUMBER	
7. AUTHOR(s) Joe Thomason, Glenn Skaggs, and John Lloyd*	8. CONTRACT OR GRANT NUMBER(s)	
9. PERFORMING ORGANIZATION NAME AND ADDRESS Naval Research Laboratory Washington, D.C. 20375	10. PROGRAM ELEMENT, PROJECT, TASK AREA & WORK UNIT NUMBERS 62712N; ZF12-151 ZF12-151-001; R02-23.701	
11. CONTROLLING OFFICE NAME AND ADDRESS Department of the Navy Office of Naval Material Washington, D.C. 20360	12. REPORT DATE August 20, 1979	
	13. NUMBER OF PAGES 55	
14. MONITORING AGENCY NAME & ADDRESS (if different from Controlling Office)	15. SECURITY CLASS. (of this report) Unclassified	
	15a. DECLASSIFICATION/DOWNGRADING SCHEDULE	
16. DISTRIBUTION STATEMENT (of this Report) Approved for public release; distribution unlimited.		
17. DISTRIBUTION STATEMENT (of the abstract entered in Block 20, if different from Report)		
18. SUPPLEMENTARY NOTES *Institute for Telecommunication Sciences		
19. KEY WORDS (Continue on reverse side if necessary and identify by block number) High-frequency radar Ionospheric models Radio-wave propagation		
20. ABSTRACT (Continue on reverse side if necessary and identify by block number) This paper describes a global ionospheric model used by NRL to analyze the performance of high-frequency radar systems. The model described is based primarily on numerical maps derived from reports by a network of vertical sounding stations. Indices for the E, F ₁ , and F ₂ layers are used to generate electron density profiles. An exponential tail is added to the E-region profile to account for D-region effects. Numerical maps of the sporadic-E indices are available but are not included in the electron density profile. This paper also describes several applications of the ionospheric model and includes an atlas of plasma frequency contour maps generated with the model.		

CONTENTS

1.0 INTRODUCTION	1
2.0 BACKGROUND	1
3.0 IONOSPHERIC INDICES PREDICTION MODEL	3
3.1 Introduction	3
3.2 The Lower Ionosphere	3
3.3 The <i>E</i> Region	3
3.4 The <i>F</i> Region	4
3.5 Summary	8
4.0 ELECTRON DENSITY PROFILE MODEL	8
4.1 Introduction	8
4.2 <i>D</i> Region	8
4.3 <i>E</i> Region	9
4.4 <i>E</i> – <i>F</i> ₂ Valley	9
4.5 <i>F</i> ₁ Region	10
4.6 <i>F</i> ₂ Region	10
5.0 APPLICATIONS	11
5.1 Anomalous Propagation Diagnostics	11
5.2 High-Frequency Radar System Performance Prediction	15
6.0 ATLAS OF PLASMA FREQUENCY CONTOUR MAPS	15
REFERENCES	52

A GLOBAL IONOSPHERIC MODEL

1.0 INTRODUCTION

The purpose of this paper is to describe a global ionospheric model used by NRL to analyze the performance of high-frequency radar systems. The basic ionospheric model was developed jointly with the Institute for Telecommunication Sciences, and was primarily based on numerical maps of ionospheric indices. These numerical maps were derived from reports by a network of ionospheric vertical sounding stations. Because the network was rather sparse in the polar region, the numerical maps do not accurately portray the polar ionosphere. The Air Force Cambridge Research Laboratory has a relatively large polar ionosphere data base which it has used to derive a set of polar corrections to the numerical maps of the F₂-layer critical frequency. These polar corrections are described in Section 3.4 and have been incorporated into the ionospheric model used by NRL. Section 5 describes some of the problems to which the ionospheric model has been applied.

Section 6 provides an atlas of plasma frequency contour maps. This atlas is a graphical representation of the ionospheric model and will be useful in providing an intuitive feeling for the model. Some simple graphical raytracing may also be carried out with these contour maps.

2.0 BACKGROUND

For many years numerous organizations, both governmental and private, have been employing the HF spectrum to communicate point-to-point between long-distance stations. It was recognized early that HF communication systems were subject to marked variations in performance, and it was hypothesized that most of these variations were directly related to changes occurring in the ionosphere. Considerable effort was made in the United States, as well as in other countries, to develop research teams for investigating ionospheric parameters and determining their effect on the nature of radio waves and the associated reliability of HF circuits. The investigators soon realized that effective operation of long-distance HF systems increased in proportion to the ability to predict variations in the ionosphere, since such an ability permitted the selection of optimum frequencies, antenna systems, and other circuit parameters that would capitalize on ionospheric variations. With the encouragement provided by these findings, it was decided that more raw ionospheric data were necessary in order to develop models that could be used to correctly anticipate ionospheric conditions affecting HF propagation. Worldwide vertical-incidence ionosondes were established which now measure values of parameters such as f_oE , F_oF_1 , f_oE_s , f_oF_2 , and $h'F$. Worldwide noise measurement records were started and steps were taken to record observed variations in signal amplitude over various HF paths. The results of this research established that ionized regions ranging from approximately 80 to 600 km above the earth's surface provide the medium of transmission for electromagnetic energy in the HF spectrum (3 to 30 MHz). Furthermore, most variations in HF system performance are directly related to changes in these ionized regions, which in turn are affected in a complex manner by solar-activity, seasonal, and diurnal variations, as well as latitude and longitude.

The Radio Propagation Unit of the U.S. Army Signal Corps provided a great deal of information and guidance in 1945 on the phenomena of HF propagation by issuing Technical Report No. 6 [1]. By 1948 a treatise of ionospheric radio propagation [2] was published by the Central Radio Propagation Laboratory of the National Bureau of Standards. This document outlined the state of the art in predicting expected maximum usable frequencies (MUF), depicted practical problems of ionospheric absorption, covered in detail acceptable methods for determining the MUF for any path at any time, and took into account the various possible modes of propagation by applying principles which were found to work in practice. The model used to make the MUF predictions employed the "two-control-point" method and assumed the ionosphere to be concentric, with reflection occurring only from the regular E and F_2 layers.

In 1950 Laitinen and Haydon of the U.S. Army Signal Radio Propagation Agency furthered the science of predicting HF system performance by developing empirical ionospheric absorption equations and combining them with the theoretical ground loss, free-space loss, and antenna gain factors. Thus, expected field strengths could be anticipated for radio signals reflecting from the E and F_2 regions, considering the effect of solar activity, seasonal, and diurnal extremes. These findings were published in Technical Report No. 9 [3].

The accumulative techniques and methods presented in the cited literature and in a number of other studies were then combined to establish effective manual methods for predicting the expected performance of HF communication systems; however, these methods were laborious and time-consuming even when only estimates for the MUF and optimum transmission frequency (FOT) were needed. To alleviate this problem, electronic computer routines were developed by such organizations as Stanford Research Institute (1957) [4], Radio Corporation of America (1961), and the Central Radio Propagation Laboratory (1961), all of which were based upon the established manual prediction methods. The CRPL program [5] was the first computerized technique that incorporated a numerical coefficient representation of the ionospheric characteristics [6]. However, only the expected MUF and FOT were predicted.

In 1962 NBS Report 7619 [7] was issued. This report outlined a computer routine that utilized the then most recent improvements in the theory of performance predictions, combining the more predictable ionospheric characteristics with circuit parameters to calculate expected HF system performance: MUF-FOT, system loss, reliability, and so forth.

In 1966 ESSA Technical Report IER-ITSA-1 [8] was published with an improved electron density model. In this model the electron density profile along the path was assumed to be adequately represented by two parabolic layers; that is, the E and F_2 layers. The height of maximum ionization, thickness, and electron density were derived for locations near the points of actual reflection along the path instead of at control points 2000 km from each end of the path.

Work beyond ITSA-1 was continued in two separate paths, one for communication analysis and predictions, reported in ITS-78 [9], and another for analysis and prediction of the performance of over-the-horizon (OTH) radar systems, reported in NRL Memorandum Reports 2226 [10] and 2500 [11]. The electron density model described in this report is a descendant of the routines developed for predicting the performance of OTH radar systems.

3.0 IONOSPHERIC INDICES MODEL

3.1 Introduction

Prediction of ionospheric indices is used extensively to estimate the performance of long-distance, HF radio systems and is useful in the design of earth-space communication systems.

The ionosphere exhibits considerable statistical variability. If the minute-to-minute variations within the hour and the day-to-day variations within the month are averaged, the remaining temporal variations, i.e., diurnal, seasonal, and solar-cycle, become quite well behaved. These remaining variations characterize what is normally referred to as the quiet ionosphere because the percentage of disturbed days in a month is usually relatively small.

It is the purpose of this section to review what indices are used to describe the quiet ionosphere; the next section will describe their use in deriving a complete electron density profile.

3.2 The Lower Ionosphere

Measurements

Information on electron densities in the lower ionosphere (50 to 90 km) is very inadequate, primarily as a result of limited observations. The technical problems of observations are formidable, and the interpretation of measurements extremely difficult.

Predictions

No *D*-region indices are included in the present prediction model. The effects of the *D* region are accounted for in the electron density model by extrapolating from the *E* region using two exponential tails; this is described in Section 4.2.

3.3 The E Region

Measurements

A large volume of vertical incidence ionosonde data has been collected over about three solar cycles, and many features of the *E* region are therefore well known. The minimum virtual height of the *E* region and the variation of maximum electron density within this region as a function of time and geographic location are readily obtained from the ionograms. The phenomenology of sporadic *E* has been investigated, but a number of problems remain unresolved.

The *E*-region indices which have been systematically scaled from the vertical-incidence ionosonde records include

<u>Index</u>	<u>Definition</u>
$f_o E$	The critical frequency of the ordinary component of the E layer; i.e., that frequency at which the signal from the ionosonde just penetrates the E layer.
$h' E_s$	The minimum virtual height of the sporadic- E layer, measured at the point where the trace becomes horizontal.
$f_o E_s$	The maximum frequency of the ordinary component of sporadic E (E_s).
$h' E$	The minimum virtual height of the E layer, measured at the point where the trace becomes horizontal.
$f_h E_s$	The blanketing frequency, i.e., the lowest ordinary wave frequency at which the E_s layer begins to become transparent, usually determined from the minimum frequency at which ordinary wave reflections of the first order are observed from a higher layer.

Predictions

The regular E layer is predicted using three indices: the monthly median value of critical frequency, the height of maximum ionization of the layer ($h_m E$), and the ratio of $h_m E$ to semi-thickness ($y_m E$). Using a numerical mapping method, Leftin has produced numerical coefficients representing $f_o E$ for computer applications on a worldwide basis. They were mapped in terms of latitude, longitude, and universal time [12]. The numerical coefficients were derived from measurements taken during 1958 (high solar activity) and 1964 (low solar activity). A linear interpolation procedure was used between the representative data for the high (sunspot number = 150) and low (sunspot number = 10) solar activity periods to obtain $f_o E$ estimates at all other phases of the solar cycle.

An examination of monthly median $h' E$ observations indicates negligible seasonal or geographic variation in the minimum virtual height of E -region ionization. A typical value is 110 km. When the lower region is included as an exponential tail of the E layer, an $h_m E$ of 110 km and a value of 5.5 for the ratio ($h_m E/y_m E$) are used.

The median, upper, and lower deciles of $f_o E_s$ are available from numerical maps [13]. However, because of its probabilistic nature, sporadic E is not included in the contour maps. The statistics of the sporadic E are used when the ionospheric model is used for virtual path tracing [10].

3.4 The F Region

Measurements

The vertical-incidence ionosonde network, with its long series of measurements over much of the world, provides the current basis for F -region predictions. The following indices have been systematically scaled from the vertical ionosonde records [14] although few stations report all of them.

<u>Index</u>	<u>Definition</u>
$f_o F_2$	The critical frequency of the ordinary component of the F_2 layer, i.e., that frequency at which the signal from the ionosonde just penetrates the F_2 layer.
$M(3000) F_2$	The ratio of the maximum useable frequency for a distance of 3000 km for the F_2 layer to the critical frequency of the layer.
$f_o F_1$	The critical frequency of the ordinary component of the F_1 layer, i.e., that frequency at which the signal from the ionosonde just penetrates the F_1 layer.
$h' F$	The minimum virtual height of the F layer, i.e., the minimum virtual height of the night F layer and the day F_1 layer. It is measured at the point where the F traces become horizontal. (In earlier years, the minimum virtual height of the night F layer was often combined with that of the day F_2 layer, the combined tabulation being designated $h' F F_2$. In these cases, the minimum virtual height of the F_1 layer, $h' F_1$, was tabulated separately.)
$h' F_2$	The minimum virtual height of the F_2 layer, measured at the point where the F_2 trace becomes horizontal.
$h_p F_2$	The virtual height of the F_2 layer corresponding to a frequency f , where $f = 0.834 f_o F_2$. This is based on the assumption of a parabolic ionization distribution, which is usually considered justified as an approximation near the maximum of the F_2 layer .

Predictions

The F_2 layer is described by three indices: monthly median values of critical frequency $f_o F_2$, height of maximum ionization $h_m F_2$, and ratio of $h_m F_2$ to semithickness $y_m F_2$. The monthly median values of $f_o F_2$ and the $M(3000) F_2$ factors are available as numerical map coefficients in terms of modified magnetic dip angle, longitude, and universal time [15]. The data for the mapping were from the years 1954 through 1958. The solar activity dependence is accounted for by a linear least squares fit between the high and low Zurich sunspot numbers. The height of maximum ionization is found by first determining $h_p F_2$, the virtual height of the F_2 layer at $0.834 f_o F_2$. A geometric formula $h_p F_2$ accurate to within 6% was described by Shimazaki [16]:

$$h_p F_2 = - 176 + 1490/M(3000) F_2. \quad (3-1)$$

The height of maximum ionization is then found by removing the retardation caused by lower region ionization:

$$h_m F_2 = h_p F_2 - \text{Ret.} \quad (3-2)$$

The formulas for retardation depend upon the assumed electron density profile of the lower layers. For example, the $D-E$ ionization can be a parabolic layer with an exponential tail, the $E-F$ valley a linear profile, and the F_1 layer, if present, a linear or parabolic ledge. The ratio $(h_m F_2 / y_m F_2)$ is given by coefficients in terms of sun's zenith angle and geomagnetic latitude [8].

The existence of the F_1 layer is given in terms of a maximum solar zenith angle; i.e., the F_1 layer exists only when the solar zenith angle is less than Z_{\max} . Ionosonde data were analyzed to produce a map of Z_{\max} [17]:

$$Z_{\max} = a_{x,1} + b_{x,1} R + (a_{x,2} + b_{x,2} R) \cos(X), \quad (3-3)$$

where the a_x 's and b_x 's are coefficients from the map for a particular month, R is the Zurich sunspot number, and X is the modified magnetic dip angle suggested by Rawer [18]. When solar zenith angle is less than Z_{\max} , $f_o F_1$ is then determined by

$$f_o F_1 = a_1 + b_1 R + (a_2 + b_2 R) \cos \chi + (a_3 + b_3 R) \cos^2 \chi \quad (3-4)$$

where the a 's and b 's are coefficients from a map for the particular month and χ is the solar zenith angle. The height of maximum ionization ($h_m F_1$) is given by

$$h_m F_1 = 165 + 0.6428 \chi, \quad (3-5)$$

where χ is given in degrees. The ratio $(h_m F_1 / y_m F_1)$ is assumed to be 4. The values thus derived for $h_m F_1$ and $y_m F_1$ are only tentative. If the height of the F_2 layer at $f_o F_1$ is lower than $h_m F_1$, then $h_m F_1$ and $y_m F_1$ are adjusted.

In the fall of 1975, NRL received from Terrance Elkins at the Air Force Cambridge Research Laboratory a computer deck containing software which could be used to "correct" the $f_o F_2$ coefficients provided by the ITS median model [6]. The polar correction software received from AFCRL has been adapted for use with the NRL ionospheric model. This software provides corrections to $f_o F_2$ as a function of magnetic index (K_p), day of the year, universal time, and geographic location. The polar corrections to the ITS median model are described in detail in AFCRL Technical Report TR-75-0549 [19]. They are summarized below.

The first correction applied is a K_p correction where δ , the correction factor, is a function of K_p only. The K_p correction is global. All of the other correction factors are applied only in the polar region. The equations for the K_p correction are

$$f_o F_2 \text{ (corrected)} = f_o F_2 (1 - \delta), \quad (3-6)$$

$$\delta = 0.025 X_N - 0.1, \quad (3-7)$$

where the term X_N is determined by the following:

If	$K_p < 0.3$,	then $X_N = 1$;
	$0.3 \leq K_p < 1.3$,	$X_N = 2$;
	$1.3 \leq K_p < 2.3$,	$X_N = 3$;
	$2.3 \leq K_p < 3.3$,	$X_N = 4$;
	$3.3 \leq K_p < 4.3$,	$X_N = 5$;
	$4.3 \leq K_p < 6.3$,	$X_N = 6$;
	$6.3 \leq K_p$,	$X_N = 7$.

Thus, a K_p value of 3, which represents a normal magnetic activity level, produces no correction. Higher magnetic activity reduces f_oF_2 . A maximum reduction of 7% occurs when $K_p \geq 6.3$.

The auroral oval correction to f_oF_2 is described in terms of magnetic activity (K_p), corrected geomagnetic time, and corrected geomagnetic latitude. Software for determining corrected geomagnetic coordinates was also obtained from AFCRL. The corrected geomagnetic coordinate system used was described by Gustafsson [20]. For the auroral oval, the correction factor α is defined such that

$$f_oF_2 \text{ (corrected)} = f_oF_2 (1 + \alpha), \quad (3-8)$$

where

$$\alpha = 0.4946ke^{-1.125k^2}. \quad (3-9)$$

Here, e is the Napierian base and k is defined by

$$k = \frac{|\lambda - \phi|}{X_1}. \quad (3-10)$$

In Eq. (3-10), λ is the corrected geomagnetic latitude in degrees and ϕ is the equatorward boundary of the auroral oval in degrees. X_1 is a function of the magnetic activity such that $4 \leq X_1 \leq 6$:

$$X_1 = 7 - K_p. \quad (3-11)$$

The auroral oval correction is applied if the corrected geomagnetic latitude of the location (λ) is greater than or equal to ϕ . This equatorward boundary of the oval is described by

$$\phi = 71.9 - 2.5 K_p - \tau, \quad (3-12)$$

where ϕ must be within the limits $\phi_N \leq \phi \leq \phi_M$, with

$$\phi_N = 68.9 - K_p - \tau, \quad (3-13)$$

$$\phi_M = 70.9 - K_p - \tau, \quad (3-14)$$

$$\tau = 5.1 \cos (15 (T_c - 1)). \quad (3-15)$$

Here, T_c is the corrected geomagnetic time in decimal hours (angle is in degrees).

The trough correction is the next to be applied. This is used only equatorward of the auroral oval and only when the solar zenith angle χ is greater than 90° (nighttime). The trough correction is not applied for corrected geomagnetic times T_c in the range $6 < T_c < 18$. For the trough correction the form of the correction factor α (applied as in Eq. (3-8)) depends on the value of k (defined in Eq. (3-10)):

$$\alpha = t_1 e^{-2.5(k-1)^2} \text{ (for } k > 1), \quad (3-16)$$

$$\alpha = 1.6487 t_1 k e^{\frac{-k^2}{2}} \text{ (for } k \leq 1), \quad (3-17)$$

where

$$t_1 = 0.2(1 + \cos(2\pi D/365))e^{(-\gamma^2/12)} \quad (3-18)$$

and D is the day of the year. The term γ is defined by Eqs. (3-19) and (3-20):

$$\gamma = T_c - 3 \text{ (for } 0 \leq T_c \leq 6), \quad (3-19)$$

$$\gamma = 27 - T_c \text{ (for } 18 \leq T_c \leq 24). \quad (3-20)$$

Note that only these two intervals need be defined since the trough correction is not applied in the interval $6 < T_c < 18$.

In the interval $90 < \chi$ (solar zenith angle) ≤ 94.6 , the factor t_1 is reduced by

$$t_1 = t_1 \frac{\chi - 90}{4.6} \quad (3-21)$$

to provide a smooth transition between the normal ionosphere and the trough.

3.5 Summary

The ionospheric indices used in this model are a minimum selection from those available. The $h'F$, F_2 maps are not used because the frequency at which they appear is not available, so it is not possible to properly adjust for retardation. In fact, if the retardation is not correctly accounted for, the bottom of the F layer occasionally will be calculated as higher than $h_m F_2$. Therefore, the map of the ratio ($h_m F_2 / y_m F_2$) is used to give consistent results. The maps of $f_o F_2$ and ratio $h_m F_2 / y_m F_2$ are from the same data base and are statistically consistent. Using the ratio guarantees that $y_m F_2$ is positive.

4.0 ELECTRON DENSITY PROFILE MODEL

4.1 Introduction

Section 3 described how a set of indices describing the vertical electron density profile is generated. This section will describe the procedure used to generate a vertical electron density profile from this set of indices. The electron density in terms of the plasma frequency squared is given by

$$N = 1.24 \times 10^{10} f_N^2, \quad (4-1)$$

where N is the number of electrons per cubic meter and f_N is the plasma frequency in MHz. Just prior to exiting from the routine, the profile is converted back to plasma frequency vs height for use in the contour mapping routines.

4.2 D Region

The profile is generated in two steps. First, the coefficients which describe the various segments are calculated and then the electron density profile is generated from these coefficients. The lower D region is considered first. The lower D layer (40 to 65 km) is given by

$$f_N^2(h) = f_N^2(40) e^{0.12(h-40)}, \quad (4-2)$$

where $f_N(40)$ is the plasma frequency at 40 km, which is assumed to be 2.01×10^{-2} MHz, and h is the height. This corresponds to an electron density of 5 electrons per cubic centimeter. This model of the lower D region was suggested by Nestorov [21].

The expression used to describe the upper D region (65 to 98 km) is an adaptation of the exponential model suggested by Nestorov:

$$f_N^2(h) = f_N^2(65) e^{k(h-65)}. \quad (4-3)$$

Rather than tie the upper exponential to the solar zenith angle as Nestorov did, the exponential coefficient k is chosen to merge the exponential upper D region with the E -region model. Thus the upper D -region model follows the diurnal and seasonal variations of the E -region model. The expression for k is

$$k = 1n\{f_N^2(98)/f_N^2(65)\}/(98 - 65), \quad (4-4)$$

where $f_N(65)$ is the plasma frequency at 65 km from the lower D -region model. $f_N(65)$ is 8.98×10^{-2} MHz. This corresponds to about 100 electrons per cubic centimeter. $f_N(98)$ is found by evaluating the E -region parabola at 98 km. The slopes of the equations used for the D layer are not continuous at the two merge points (65 and 98 km). This produces cusps at these points in the virtual height profile. However, the electron density is sufficiently low at these points so that the cusps do not significantly affect the direction of rays in the high-frequency range.

4.3 E Region

The ionospheric indices used are f_oE , median (ordinary-ray) critical frequency of the E layer; h_mE , height of maximum ionization of the E layer (110 km); and y_mE , the E -layer semithickness (20 km). The electron density (proportional to plasma frequency squared) is modeled as a parabola:

$$f_N^2(h) = (f_oE)^2 \left[1 - \left(\frac{h_m E - h}{y_m E} \right)^2 \right], \quad (4-5)$$

where $f_N(h)$ is the plasma frequency at a height h .

4.4 E - F₂ Valley

Normally there is a valley in the distribution of electron density between the E and F_2 regions. Only the total density in this valley is modeled, not the shape. In this area between the E and F_2 regions the electron density is modeled by a straight line between a point on the top side of the E -region parabola and a point on the lower side of the F_2 -region parabola. These two points are both defined in terms of the f_oE . The point on the top side of the E -region parabola is at $0.8516 f_oE$. The point on the bottom side of the F_2 -region parabola is at $0.98 f_oE$. The height h_u of the upper point is

$$h_u = h_m F_2 - y_m F_2 \sqrt{1 - \left(\frac{0.98 f_oE}{f_o F} \right)^2}. \quad (4-6)$$

The height h_L of the lower point is

$$h_L = h_m E + y_m E \sqrt{1 - \left(\frac{0.8516 f_oE}{f_o E} \right)^2}. \quad (4-7)$$

The constants 0.8516 and 0.98 have been chosen to represent as nearly as possible measured depths of the valley.

4.5 F_1 Region

The F_1 layer is described by three parameters: the critical frequency ($f_o F_1$), the height of maximum ionization ($h_m F_1$), and the semithickness ($y_m F_1$). The F_1 layer may be either linear or parabolic. If linear,

$$f_N^2(h) = S_1 (h - h_m F_1 + y_m F_1), \quad (4-8)$$

where S_1 is the slope defined by

$$S_1 = \frac{(f_o F_1)^2}{y_S}. \quad (4-9)$$

The term y_S is defined by

$$y_S = h_2 - h_m F_1 + y_m F_1 \quad (4-10)$$

or

$$y_S = 1,$$

whichever is larger. The term h_2 is height in the F_2 layer at $f_o F_1$:

$$h_2 = h_m F_2 - y_m F_2 \sqrt{1 - \left(\frac{f_o F_1}{f_o F_2}\right)^2}. \quad (4-11)$$

If the F_1 layer is parabolic,

$$f_N^2(h) = (f_o F_1)^2 \left[1 - \left(\frac{h_m F_1 - h}{y_m F_1} \right)^2 \right]. \quad (4-12)$$

The choice of a linear or parabolic shape to the electron density of the F_1 layer is made by comparing the height of maximum ionization of the F_1 layer ($h_m F_1$) to the F_2 -layer height at $f_o F_1$ (h_2 as defined by Eq. (4-11)). If h_2 is higher than $h_m F_1$, then the parabolic layer, Eq. (4-12), is used for the F_1 layer. If h_2 is not higher than $h_m F_1$, the slope S_1 defined by Eq. (4-8) is compared with the slope S_2 of the F_2 layer at the point h_2 (frequency is $f_o F_1$):

$$S_2 = \frac{2(f_o F_2)^2 (h_m F_2 - h_2)}{(y_m F_2)^2}. \quad (4-13)$$

If the difference ($S_1 - S_2$) is positive, the linear F_1 layer is used. If the difference is negative, the parabolic layer is used.

4.6 F_2 Region

The ionospheric parameters used for this region are the median critical frequency ($f_o F_2$), the height of maximum ionization ($h_m F_2$), and the semithickness ($y_m F_2$). The nose of the F_2 layer is described by

$$f_N^2(h) = (f_o F_2)^2 \left[1 - \left(\frac{h_m F_2 - h}{y_m F_2} \right)^2 \right]. \quad (4-14)$$

The top side of the F_2 region is modeled by merging a single exponential to the top of the F_2 layer at a height h_t determined by the relation

$$h_t = h_m F_2 + 0.25 y_m F_2. \quad (4-15)$$

Above height h_t the plasma frequency $f_N(h)$ is described by the equation

$$f_N^2(h) = \frac{k(f_o F_2)^2 e^{-\left[\frac{h-h_t}{k}\right]}}{2y_m F_2}, \quad (4-16)$$

where

$$k = 1.875 y_m F_2 \quad (4-17)$$

This top-side model is an adaptation of one developed by Bent, et al. [22].

The value of k is chosen to make the F_2 -region parabola (Eq. (4-14)), the top-side exponential (Eq. (4-16)), and their derivatives continuous at h_t , the merge point. This is done to keep from causing a cusp at the merge point in the virtual height profile.

5.0 APPLICATIONS

5.1 Anomalous Propagation Diagnostics

Plasma frequency contour maps can be used to predict when anomalous propagation conditions may occur. For example, the contour map shown in Fig. 1 exhibits a definite positive tilt from the origin out to about 2700 n.mi. Line of sight at zero elevation angle is shown on the contour map with a broken line. Since low-elevation-angle rays are more likely to become trapped, tilts in the immediate vicinity of this broken line are critical for trapping during the first refraction. An estimate of the operating frequency which will produce elevated modes for a particular contour map can be obtained by finding the highest plasma frequency encountered by the zero elevation-angle line of sight and using the well known secant law to estimate the equivalent oblique frequency f_o :

$$f_o = f_v \sec \phi, \quad (5-1)$$

where f_v is the vertical plasma frequency and ϕ is the angle between the ray line of sight and the zenith at the true height of reflection. When the elevation angle is zero, the angle ϕ may be found by solving

$$\sin \phi = \frac{R}{R + h}, \quad (5-2)$$

where R is the earth radius and h is the true height of reflection. Making use of the identity $\sin^2 \phi + \cos^2 \phi = 1$, Eq. (5-1) may be rewritten

$$f_o = k f_v, \quad (5-3)$$

where k is defined by the expression

$$k = \sqrt{\left[1 - \left(\frac{R}{R + h}\right)^2\right]^{-0.5}}. \quad (5-4)$$

Following the broken line in Fig. 1 upward from the origin, we find that the vertical plasma frequency increases until it reaches a maximum of about 5.5 MHz at 280 km. Equation (5-3) may be used to predict the critical frequency for the zero-elevation-angle ray. In this case we would estimate that at operating frequencies above 19.2 MHz all rays would penetrate and that at operating frequencies below 19.2 MHz the low-angle rays would be refracted. Because of the positive tilt in that region of the ionosphere where these rays are refracted, the low-angle rays will probably be tilted into an elevated propagation mode.

The trajectory of the zero-elevation-angle ray may be predicted in greater detail by using a raytracing program with a numerical representation of the contour maps. The contour map shown in Fig. 1 was used with the raytracing routine developed by Jones and Stephenson [23] to trace the low-elevation-angle rays. Interface between the raytracing program and the plasma-frequency contour map was accomplished by an adaptation of an interpolation routine written by ARCON Corporation for AFCRL [24]. This routine supplies plasma frequency and the required spacial derivatives when a grid of plasma-frequency vertical profiles is input. For an operating frequency of 19 MHz and the ionosphere shown in Fig. 1, the raytracing program predicts that the zero-elevation-angle ray will reach a maximum altitude of 276 km at 1170 n.mi. before being refracted back toward the earth. During the first refraction the ray will be tilted sufficiently to miss the earth. The point of closest approach of the ray to the earth between the first and second refractions is 113 km at 2000 n.mi. Figure 2 shows graphically the trajectory of rays between 0° and 10° elevation.

The point of all this is not that the propagation mode predicted will be duplicated precisely but that elevated modes of the type predicted by the raytracing routine may be expected for the combination of operating conditions examined.

When used for raytracing, the ionospheric model must be used with a magnetic field model. Typically, the earth-centered dipole model provided with the Jones-Stephenson raytracing program is employed. In this model the gyrofrequency f_H is given by

$$f_H = f_H' \left(\frac{R}{R+h} \right)^3 (1 + 3 \cos^2 \theta)^{0.5}, \quad (5-5)$$

where f_H' is the gyrofrequency at the equator on the ground (typically 0.8 MHz); R is the radius of the earth; h is the height above the earth; and θ is the geomagnetic colatitude. The magnetic dip angle I is given by

$$\tan I = 2 \cot \theta. \quad (5-6)$$

Occasionally the calculation of absorption in conjunction with raytracing is desired. The Jones-Stephenson raytracing routine provides this option. The software package supplied with the basic raytracing routine includes several collision frequency models. Typically the simple exponential profile (EXPZ) is used where the collision frequency ν is defined by

$$\nu = \nu_0 e^{-\alpha(h-h_0)}, \quad (5-7)$$

where h is height above the ground; h_0 is the reference height (typically 70 km); ν_0 is the collision frequency at the reference height (typically 8×10^6 collisions per second); and α is the exponential decay coefficient (typically 0.16).

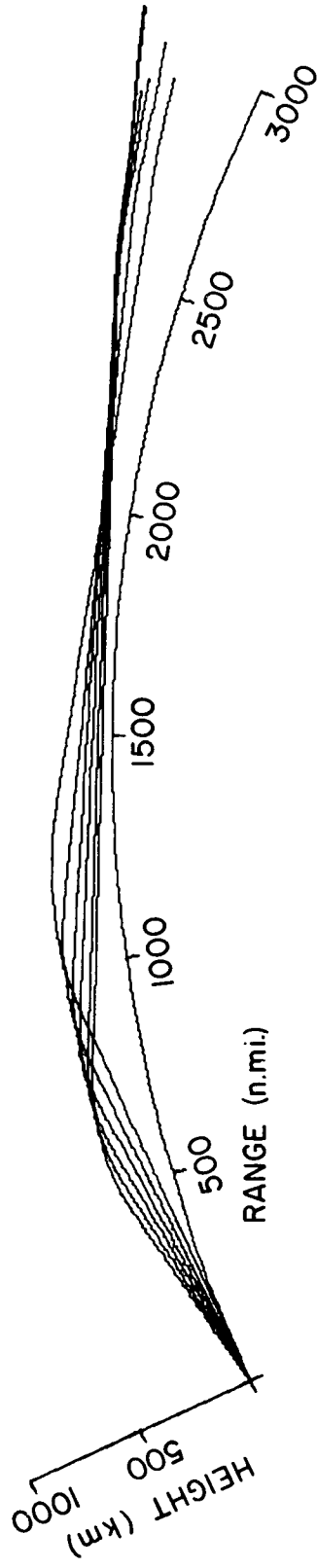


Fig. 2 — Example of raytrace showing elevated mode

Comparisons have been made between the loss predicted by the raytracing routine and that predicted by virtual path tracing. For example, for a test case where the sunspot number was 28 and the solar zenith angle was 63° , the virtual path tracing model [10] predicted 39-dB one-way nondeviative (*D* region) absorption loss for a 1° elevation-angle ray at 5 MHz. This same program also calculates deviative absorption which occurs as the ray penetrates deeper into the ionosphere and deviates from a line-of-sight path. For the test case, the deviative absorption was 6 dB, making a total absorption loss of 45 dB. Using the ionospheric model described in this report with the Jones-Stephenson raytracing routine, the total absorption loss calculated for the test case was 41 dB. This level of agreement between the two programs gives some confidence in the *D*-region models used. However, there remains one major defect in using the Jones-Stephenson raytracing routine with this ionospheric model for loss calculations. Because of the probabilistic nature of the sporadic *E*, this layer is not handled correctly by the raytracing routine, which is basically deterministic. In the virtual path tracing program a separate loss calculation is made for the effect of sporadic *E*. This loss is termed obscuration loss and is applied to *F*-layer modes in the virtual path tracing program. The addition of this feature to our version of the Jones-Stephenson raytracing routine is planned.

5.2 High-Frequency Radar System Performance Prediction

The global ionospheric model may be used to predict the performance of high-frequency OTH radar systems. This requires that a model of the radar be coupled to the ionospheric model. NRL Memorandum Reports 2226 [10] and 2500 [11] describe how an earlier version of the ionospheric model was used for this purpose. This procedure makes use of virtual path tracing and therefore will not describe as completely the propagation modes associated with any specific set of conditions. This is especially true during transition when anomalous propagation modes exist. For these modes, the ionospheric model should be used with the Jones-Stephenson raytracing program as described in the previous section.

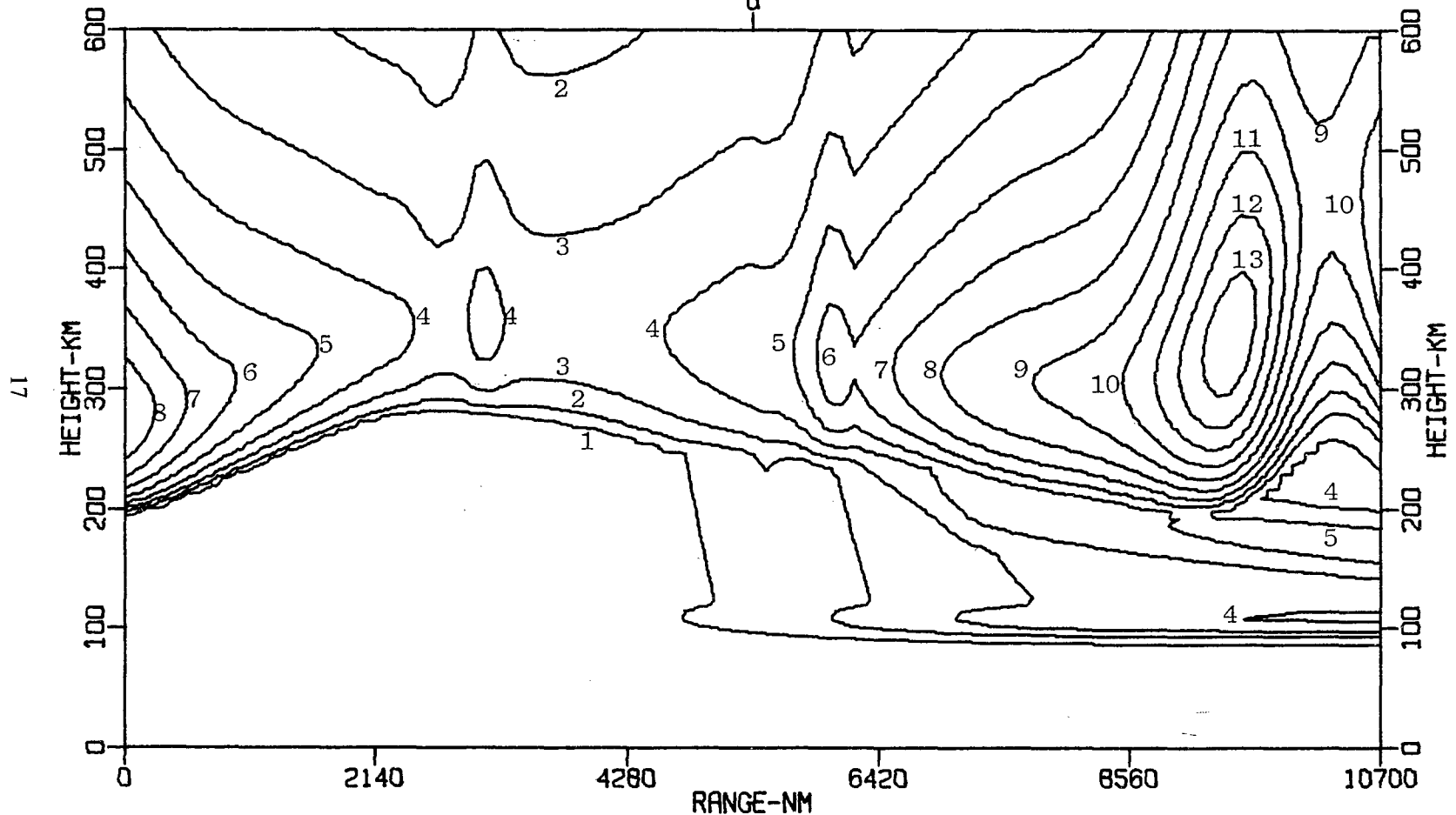
6.0 ATLAS OF PLASMA FREQUENCY CONTOUR MAPS

To provide a graphic picture of how the plasma frequency varies as a function of location, season, time of day, and magnetic activity, a set of plasma frequency contour maps are included (Figs. 3-38). All of these contour maps begin at the equator, follow the 69° W meridian north through the north geographic pole, and then south along the 111° E meridian back to the equator. Thus each contour map provides a cross section of the entire northern hemisphere. Maps are provided for three seasons, equinox (represented by March), summer (represented by June), and winter (represented by December). For each season, contours were mapped for 0500 UT, 1100 UT, 1700 UT, and 2300 UT. These times correspond roughly to midnight, morning, noon, and evening local time along the 69° meridian. For each combination of time and season, contours were drawn without the polar corrections, and with the polar corrections for two levels of magnetic activity ($K_p = 3$ and $K_p = 7$).

PLASMA FREQUENCY CONTOURS

LOCAL TIME

0



MAR GMT = 500 SSN = 70 BER = 0.0

Fig. 4 - March map, 0500 UT, polar corrections ($K_p = 3$)

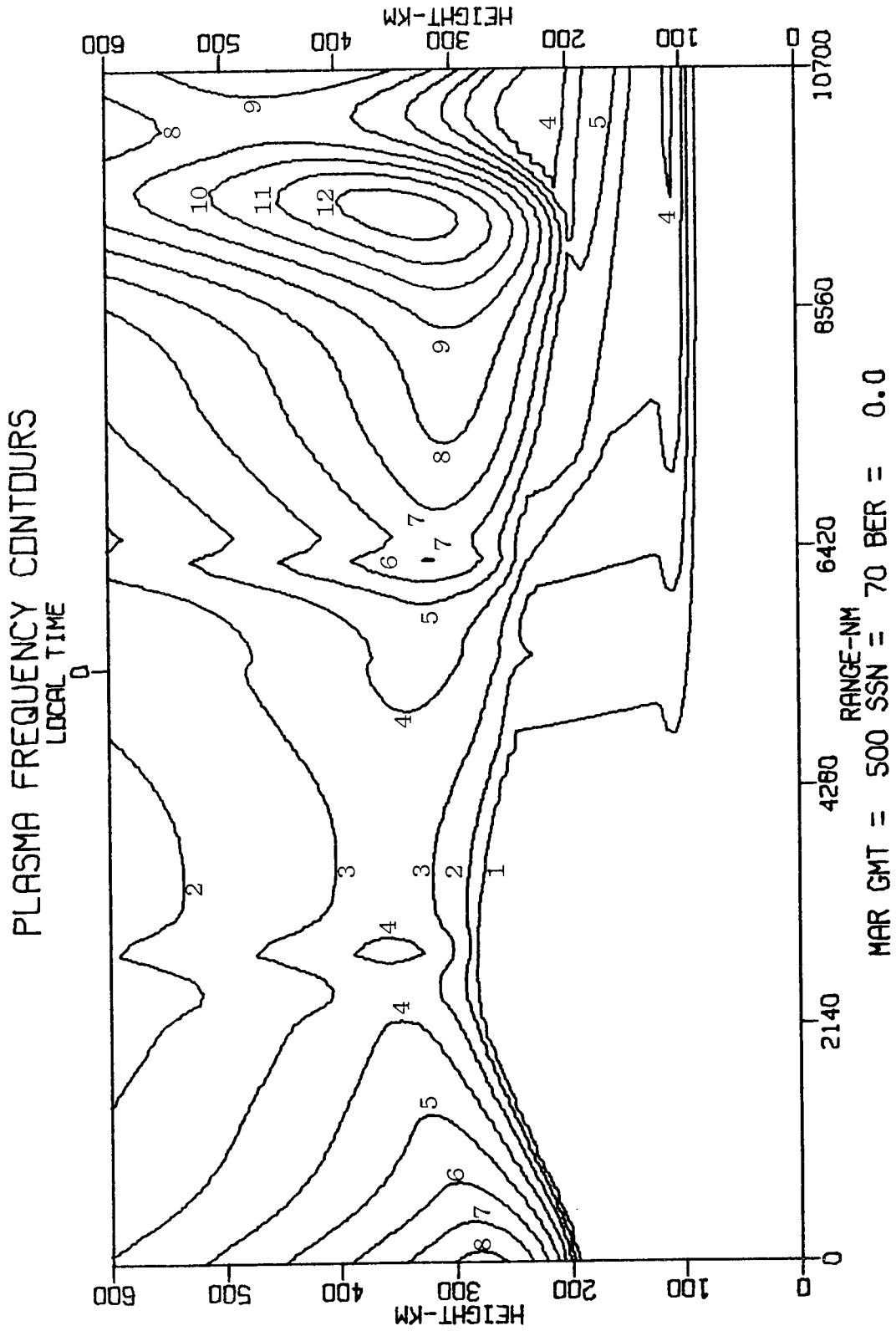


Fig. 5 — March map, 0500 UT, polar corrections ($K_p = 7$)

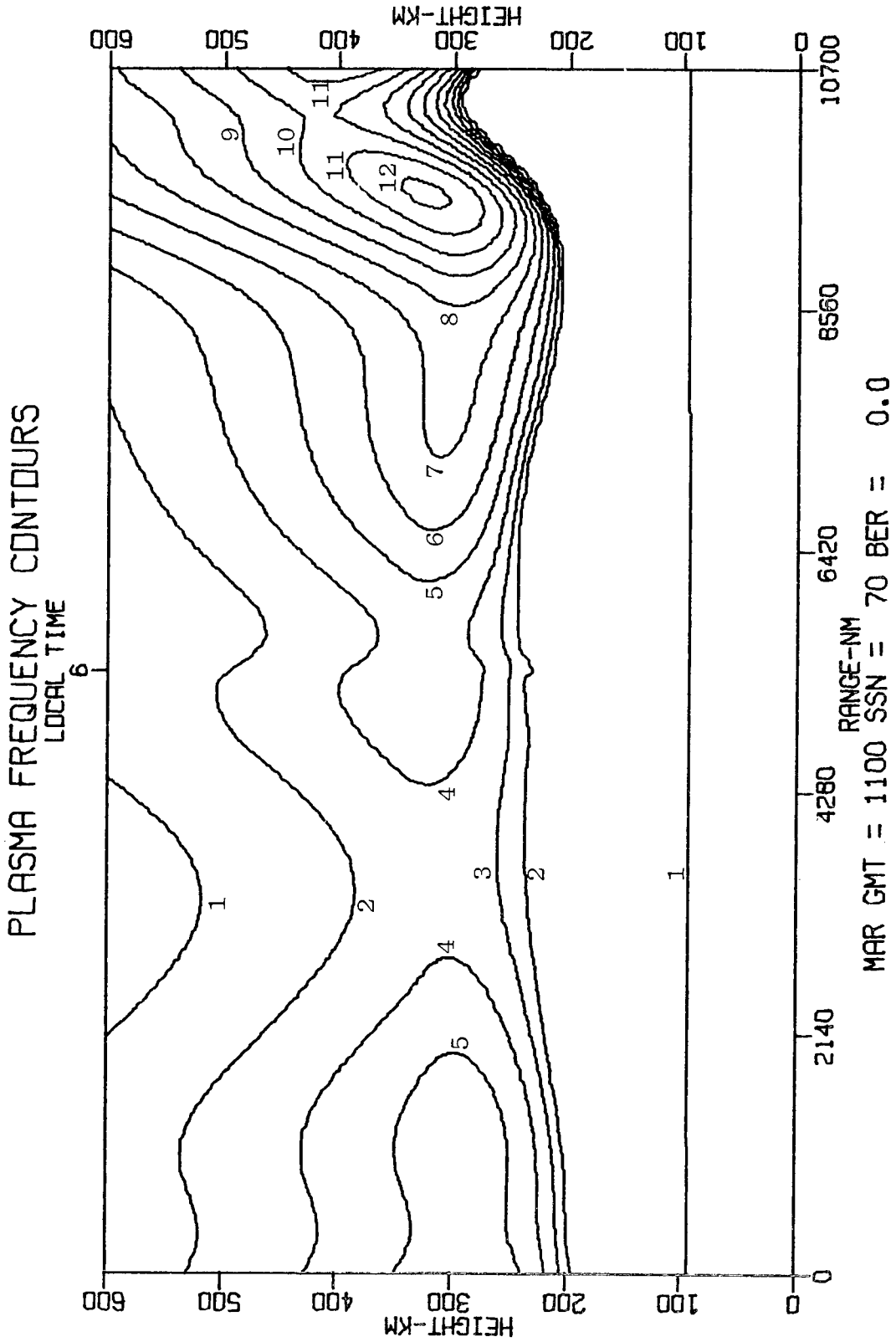
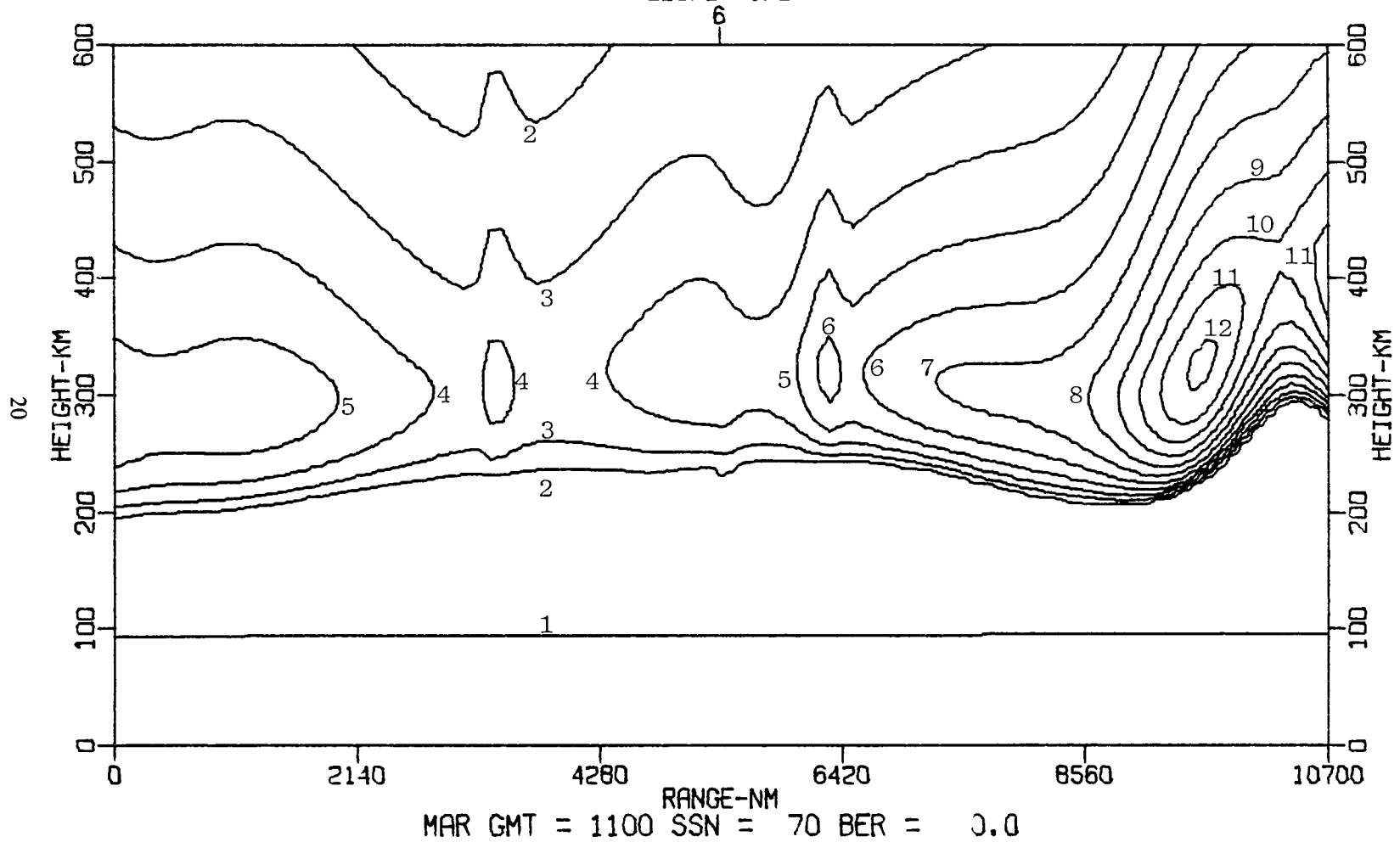


Fig. 6 — March map, 1100 UT, no polar corrections

PLASMA FREQUENCY CONTOURS

LOCAL TIME

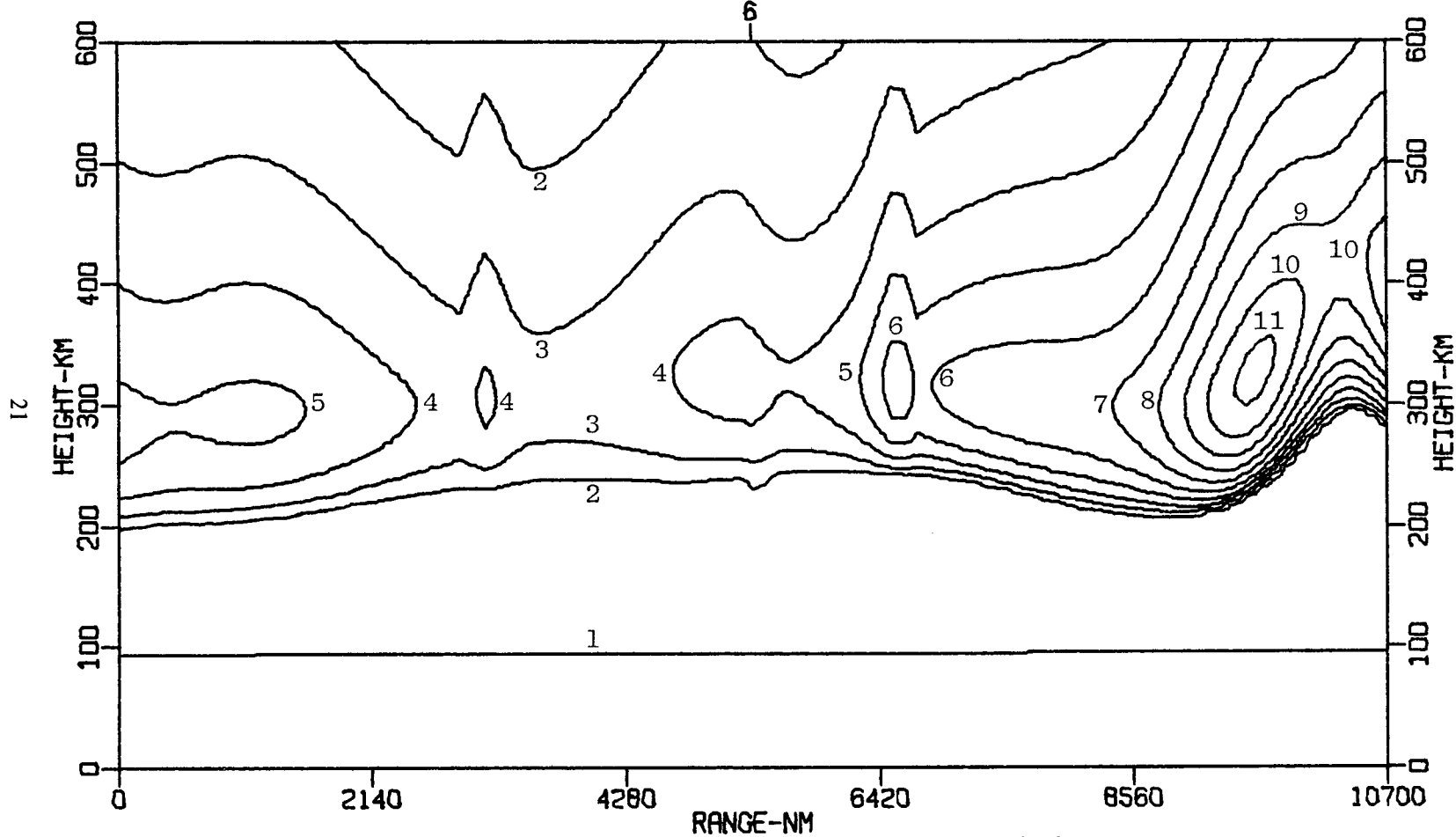


THOMASON, SKAGGS, AND LLOYD

Fig. 7 - March map, 1100 UT, polar corrections ($K_p = 3$)

PLASMA FREQUENCY CONTOURS

LOCAL TIME



MAR GMT = 1100 SSN = 70 BER = 0.0

Fig. 8 - March map, 1100 UT, polar corrections ($K_p = 7$)

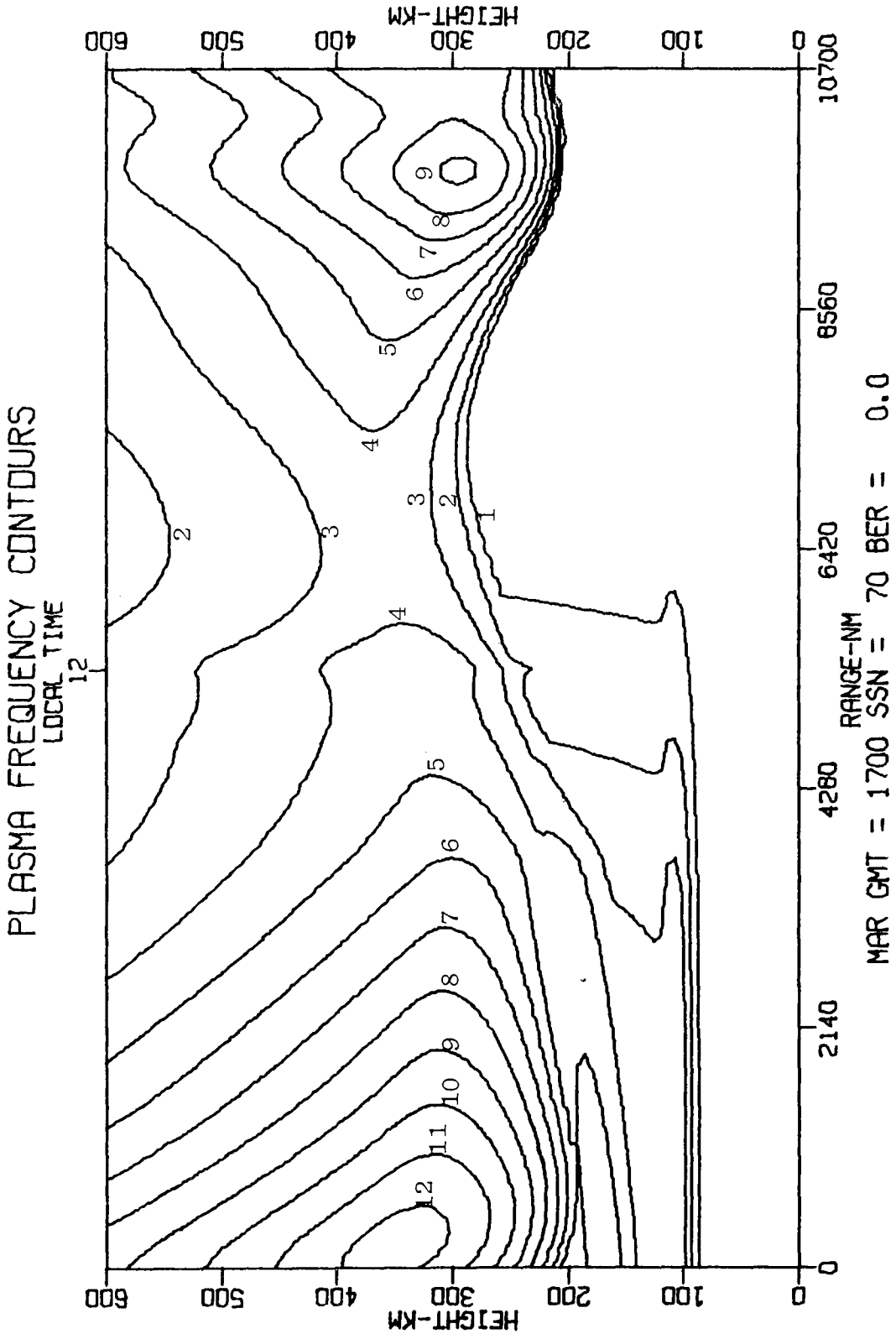


Fig. 9 - March map, 1700 UT, no polar corrections

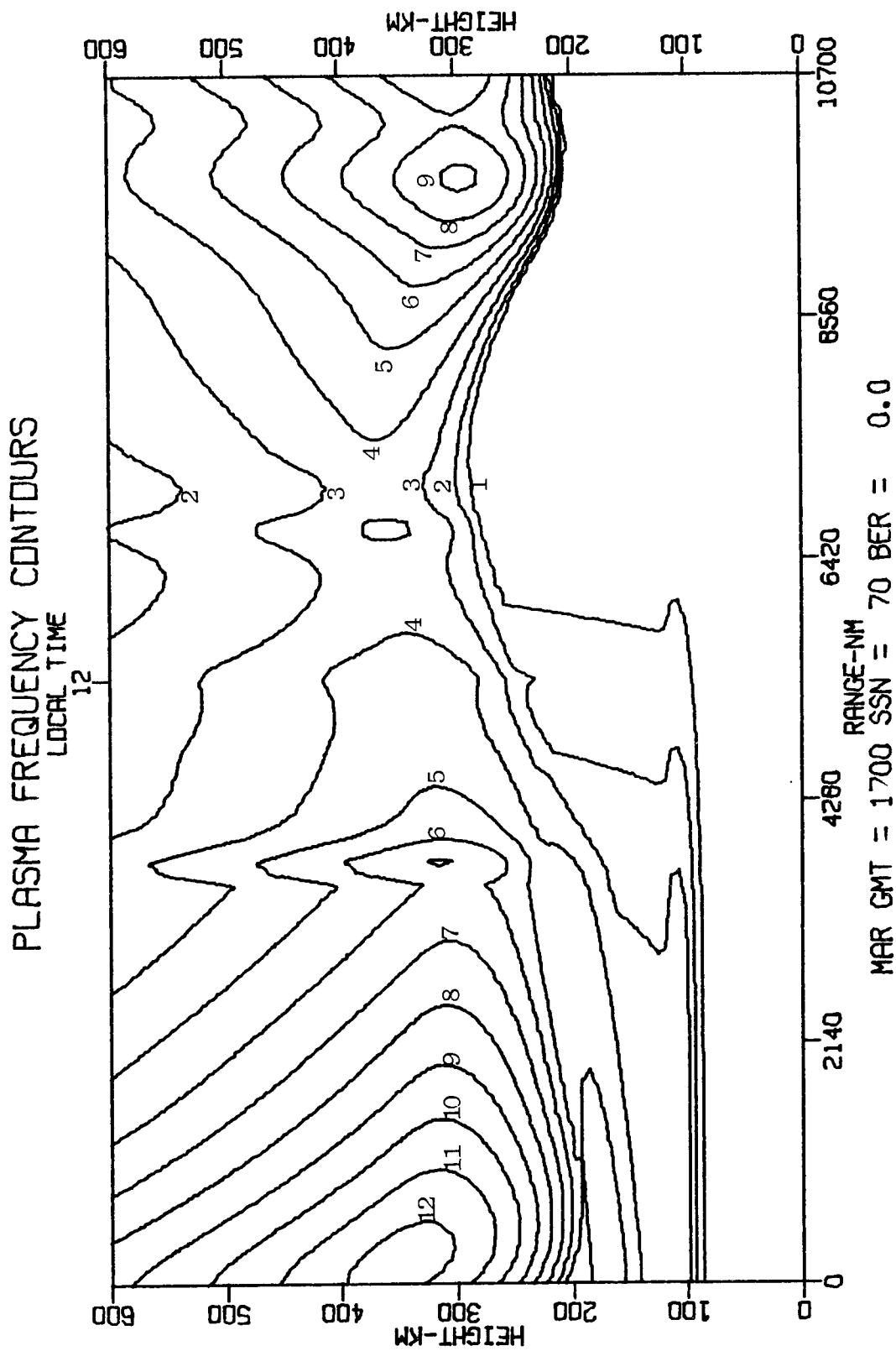
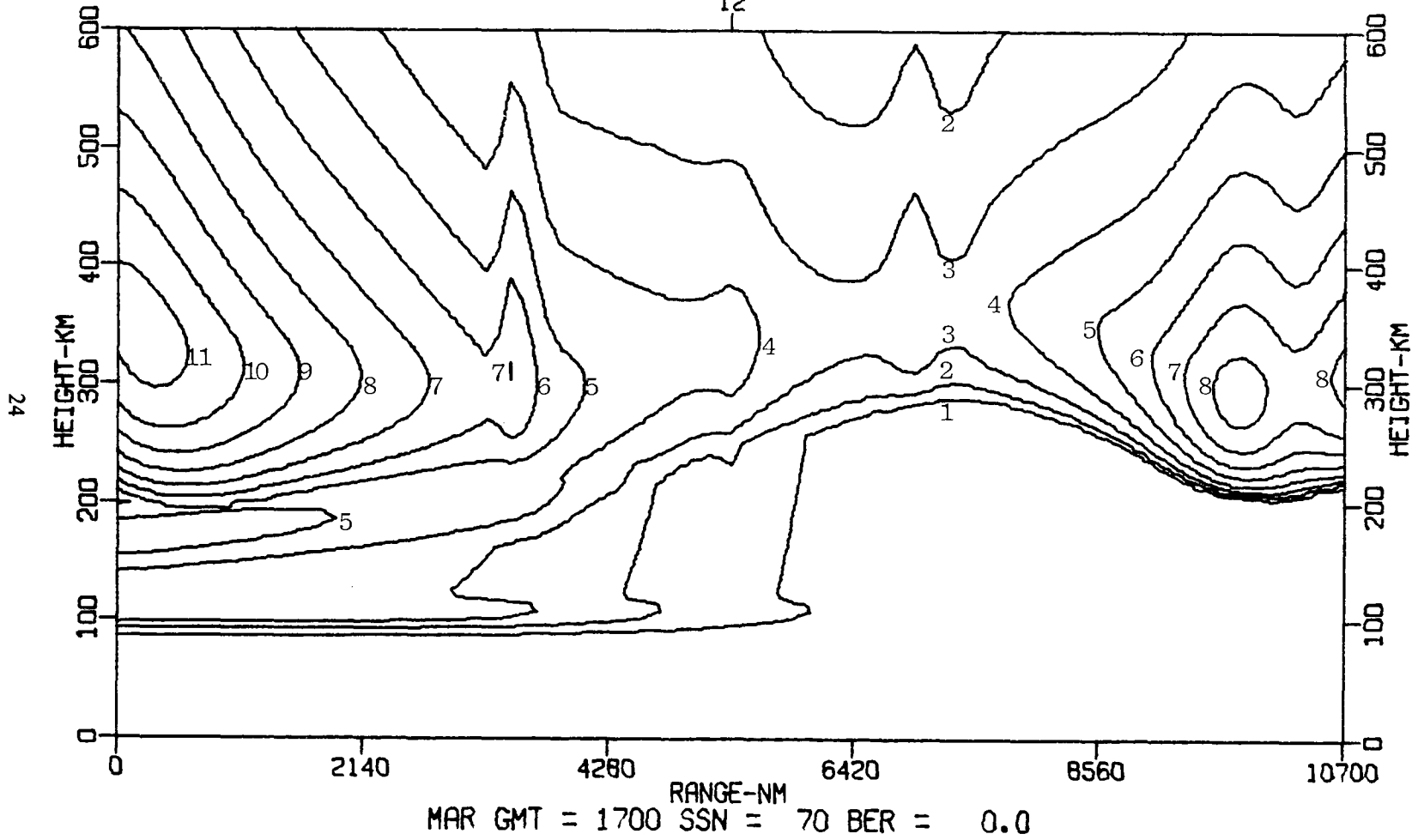


Fig. 10 — March map, 1700 UT, polar corrections ($K_p = 3$)

PLASMA FREQUENCY CONTOURS

LOCAL TIME

12



THOMASON, SKAGGS, AND LLOYD

Fig. 11 - March map, 1700 UT, polar corrections ($K_p = 7$)

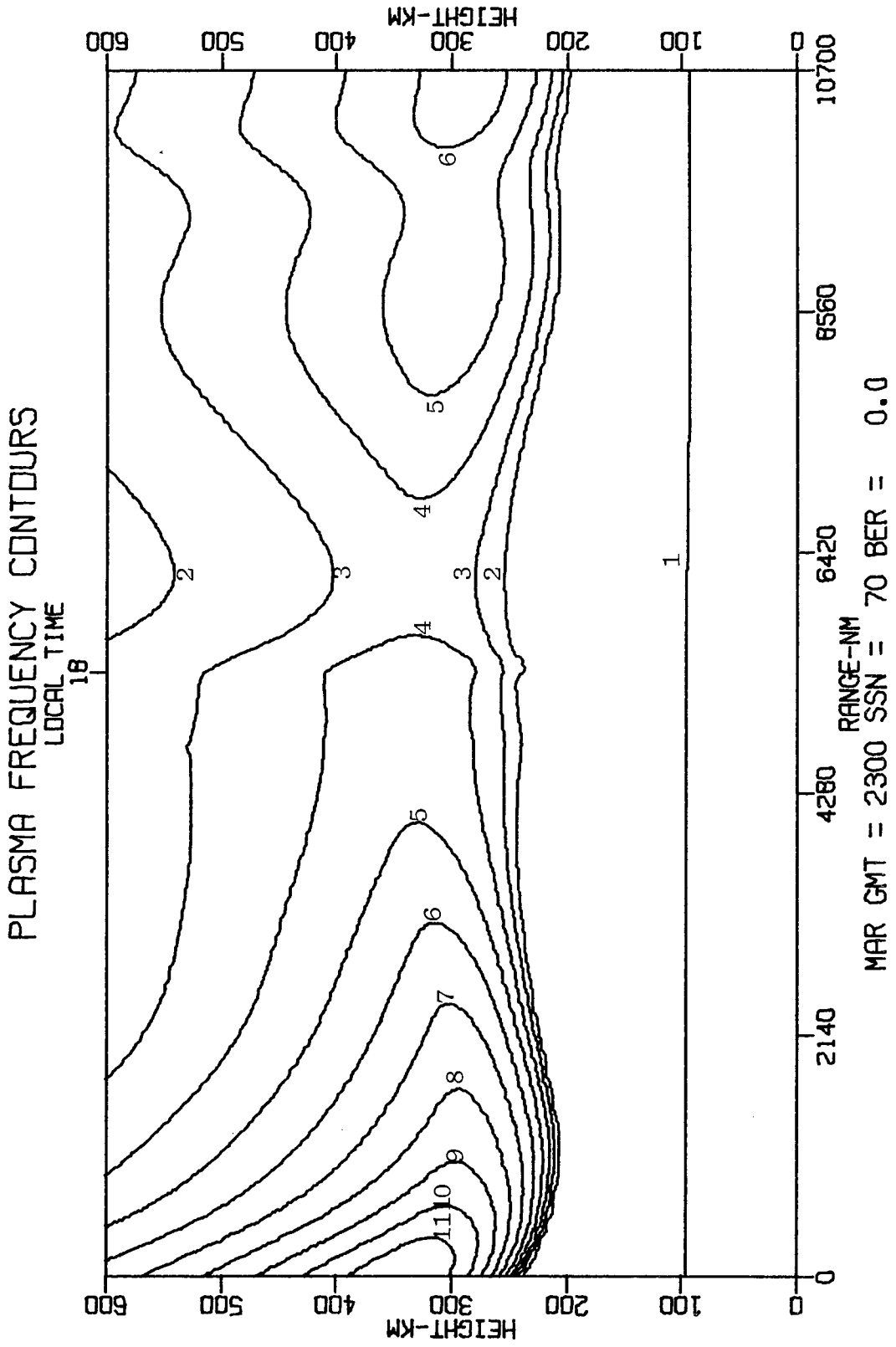


Fig. 12 - March map, 2300 UT, no polar corrections

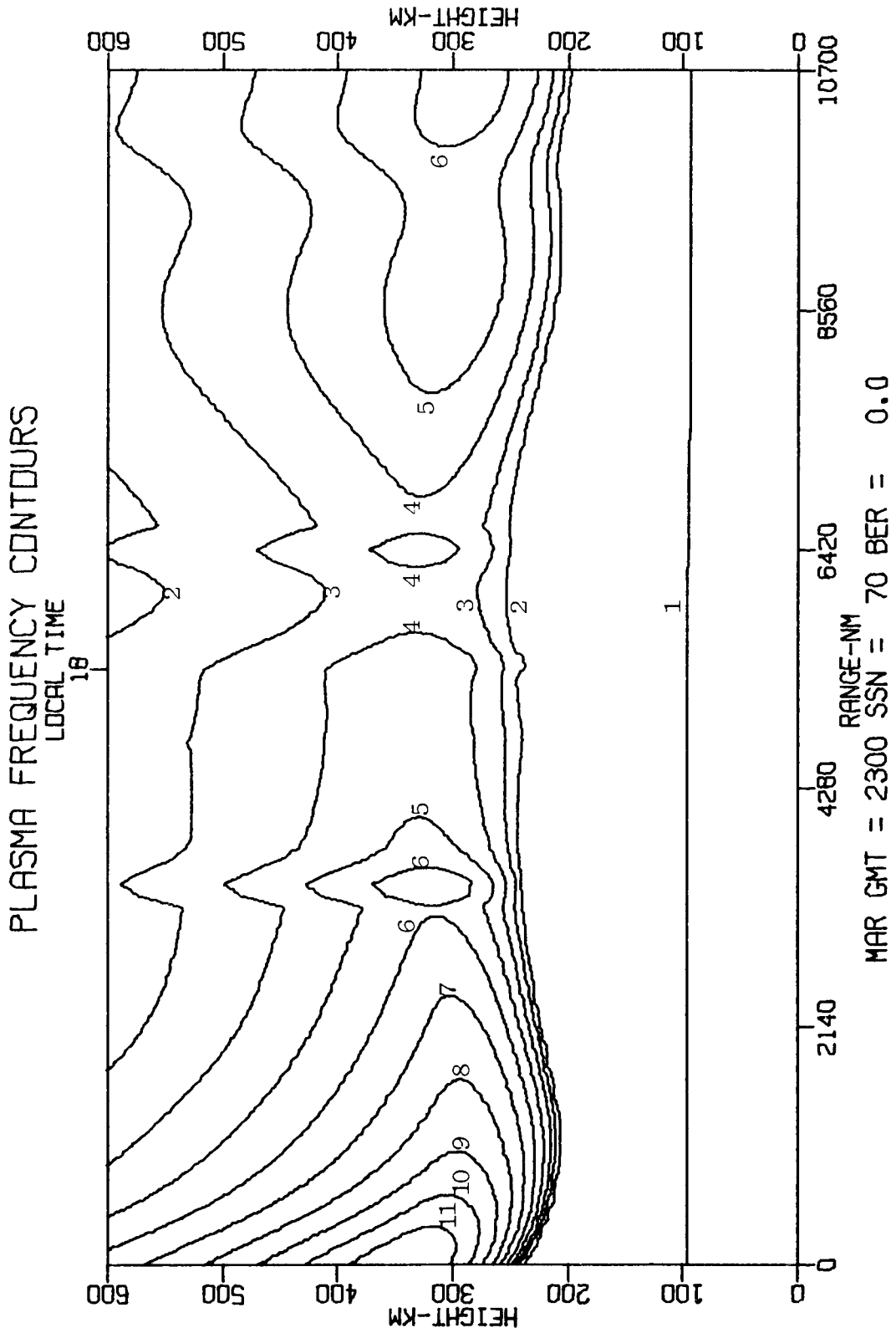


Fig. 13 — March map, 2300 UT, polar corrections ($K_p = 3$)

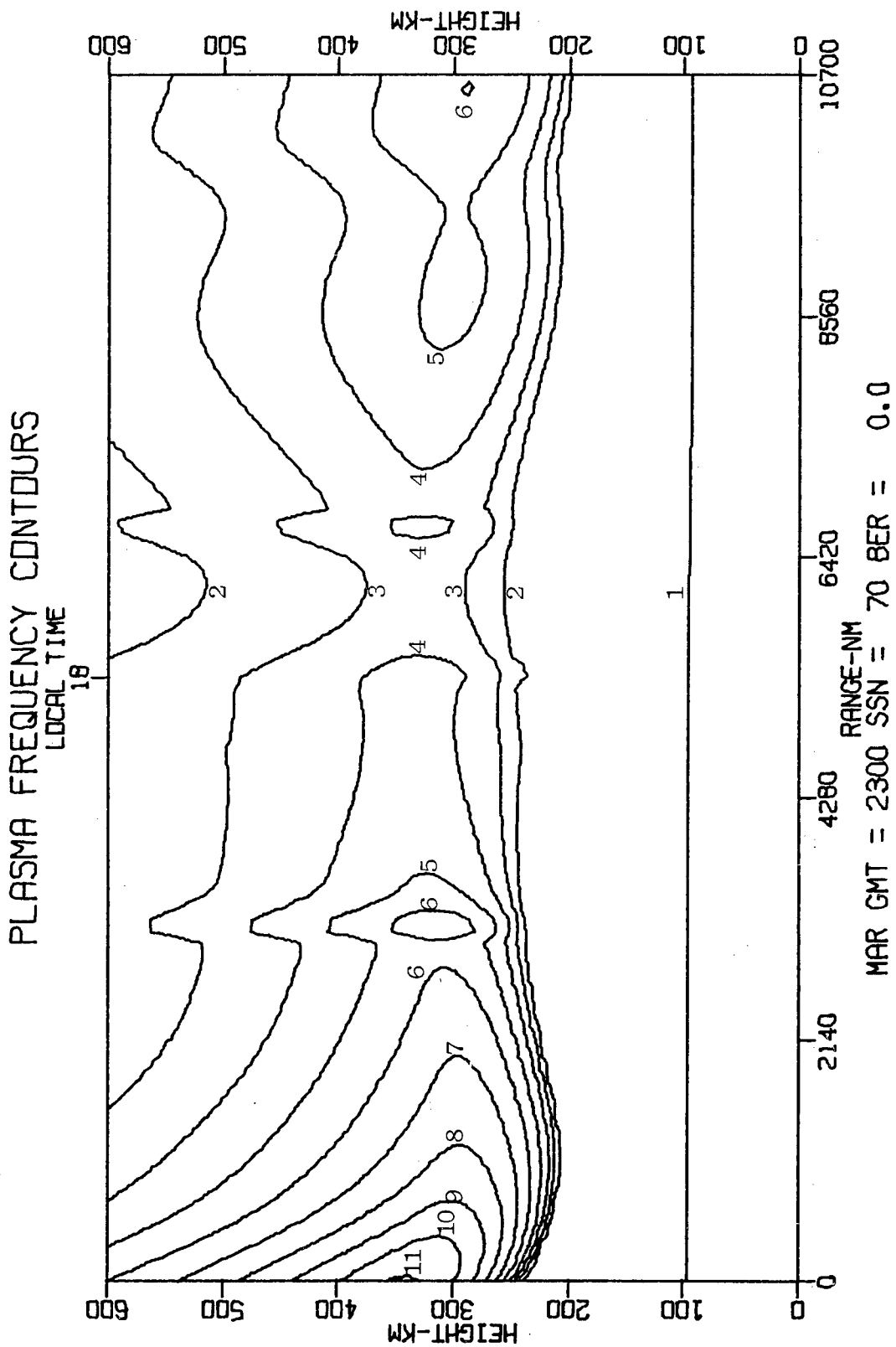


Fig. 14 - March map, 2300 UT, polar corrections ($K_p = 7$)

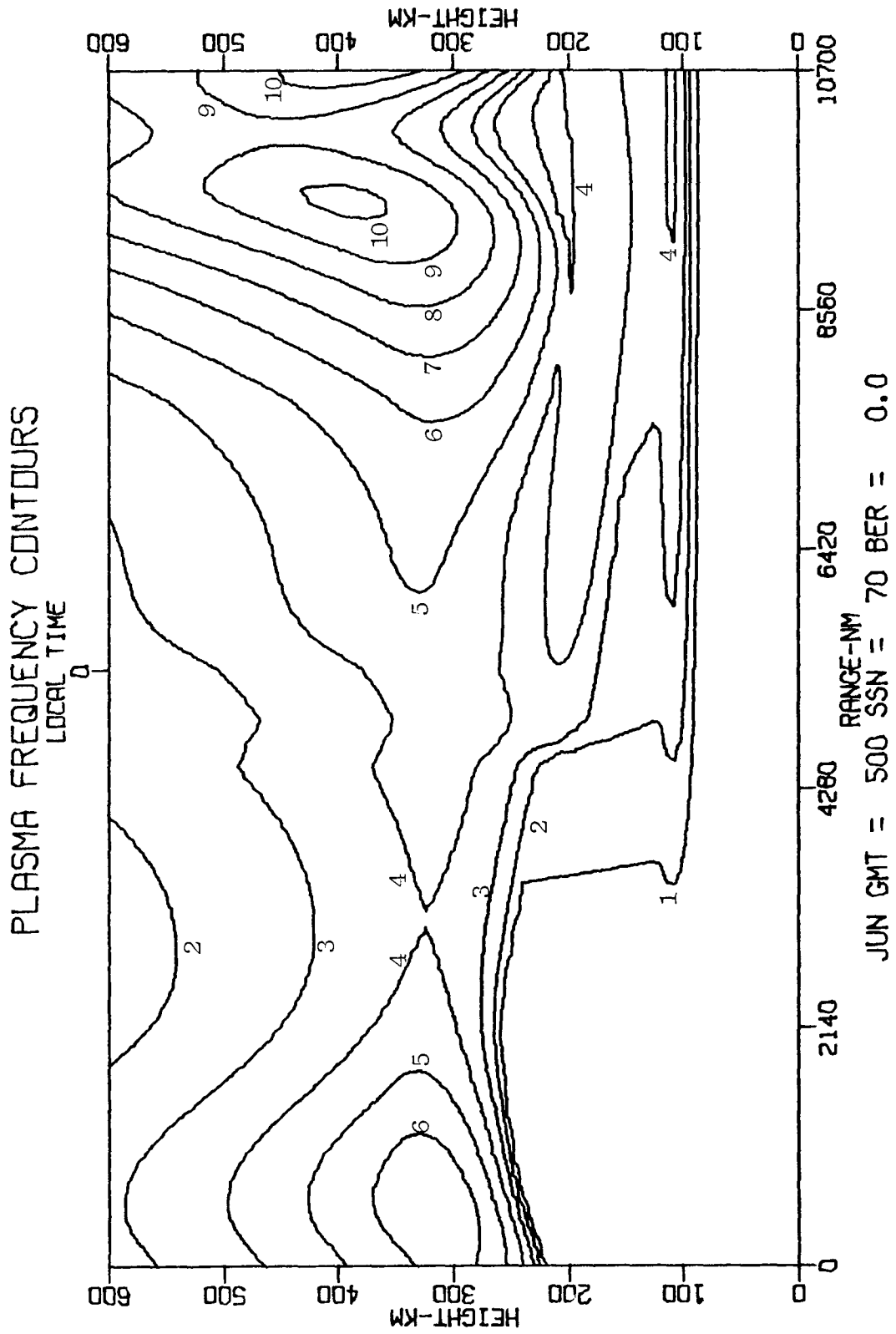


Fig. 15 — June map, 0500 UT, no polar corrections

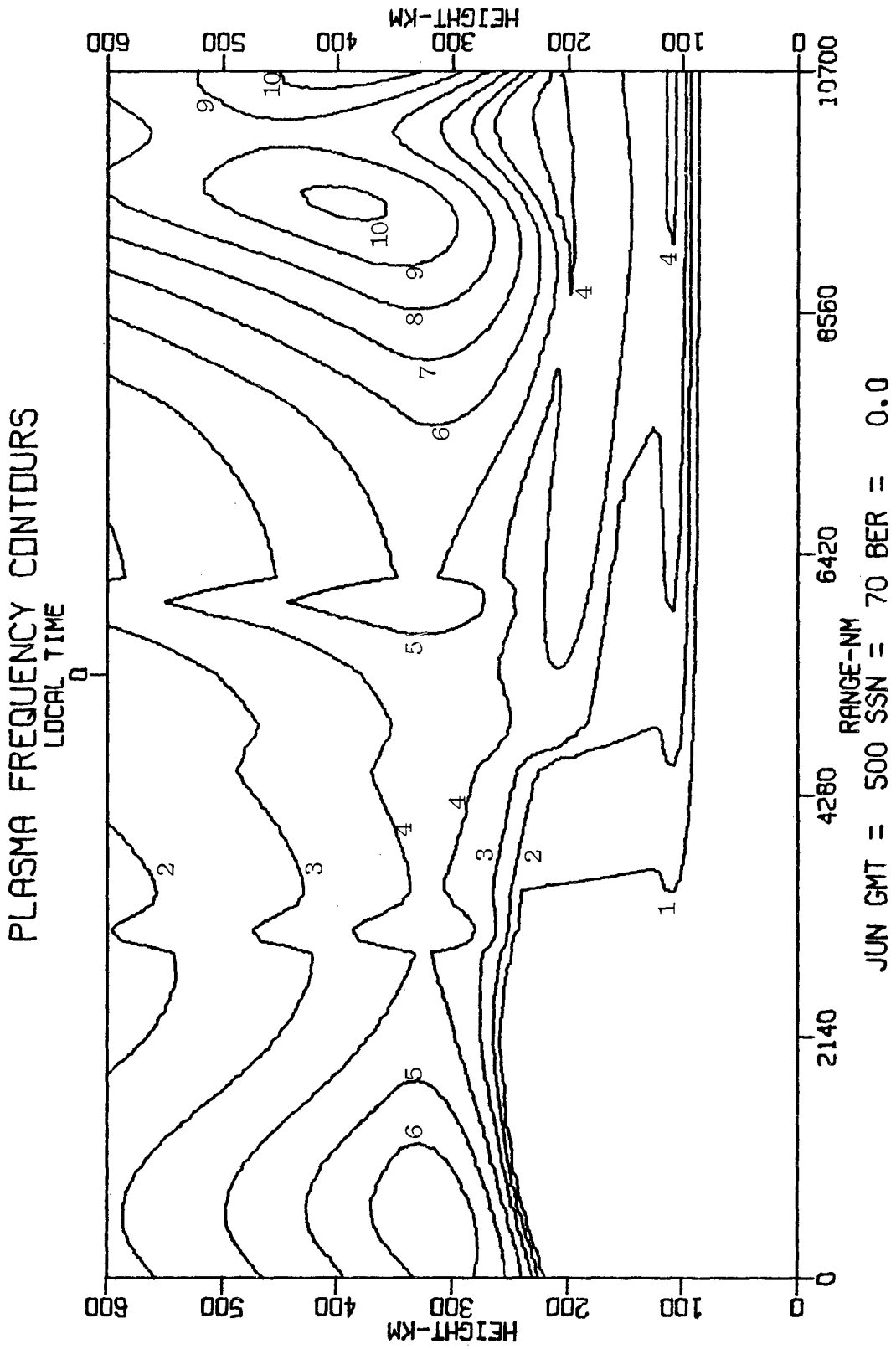


Fig. 16 — June map, 0500 UT, polar corrections ($K_p = 3$)

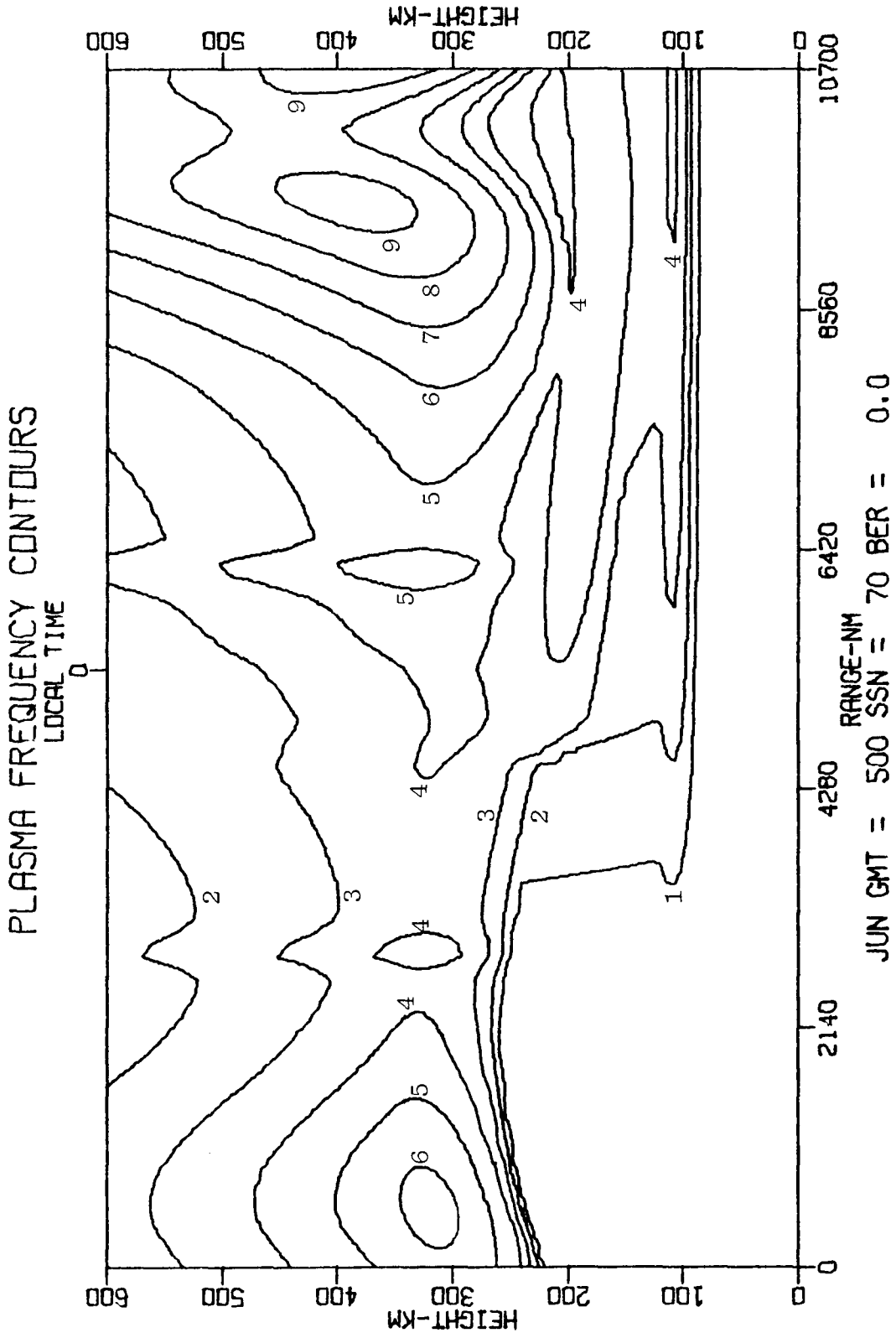


Fig. 17 — June map, 0500 UT, polar corrections ($K_p = 7$)

PLASMA FREQUENCY CONTOURS

LOCAL TIME

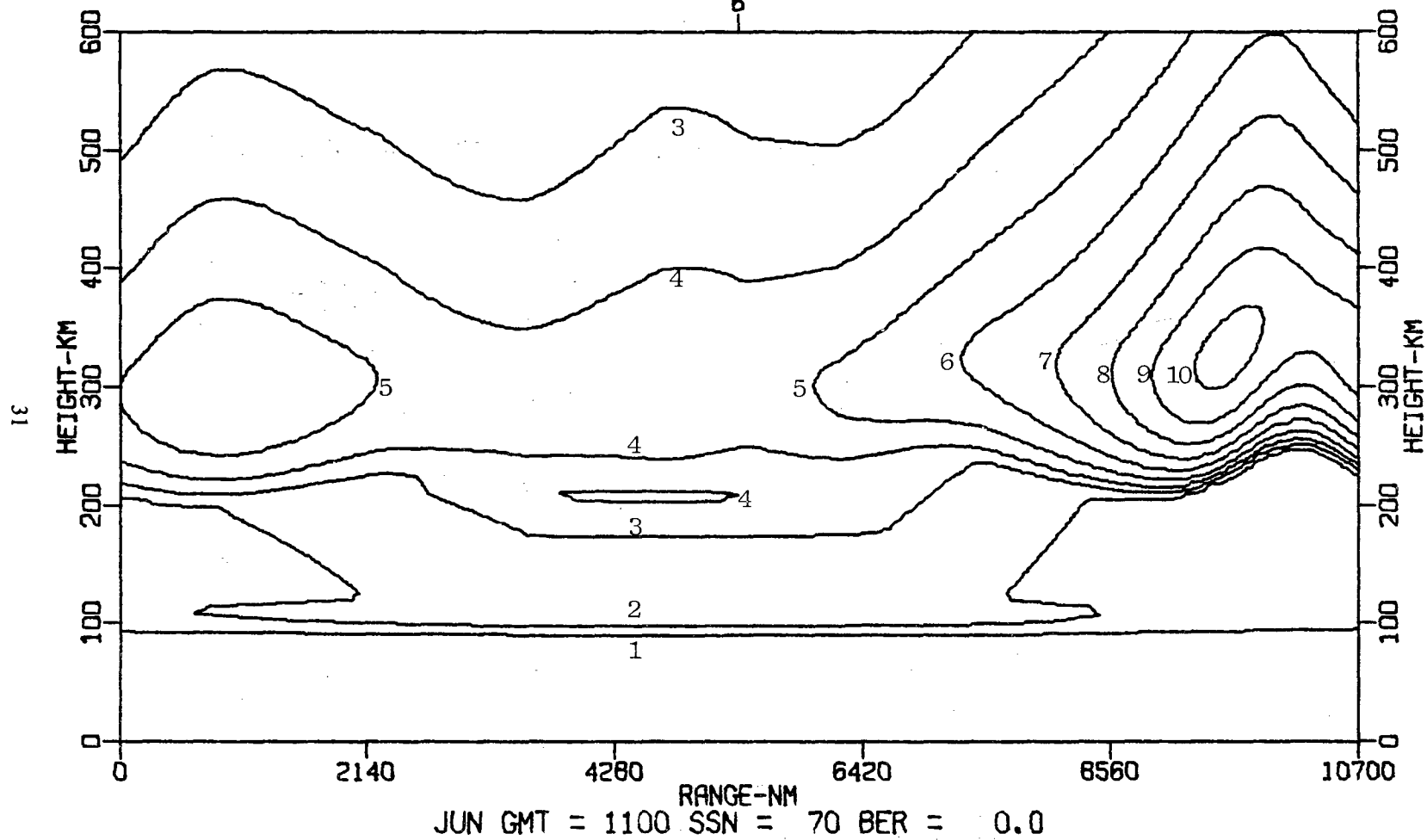


Fig. 18 - June map, 1100 UT, no polar corrections

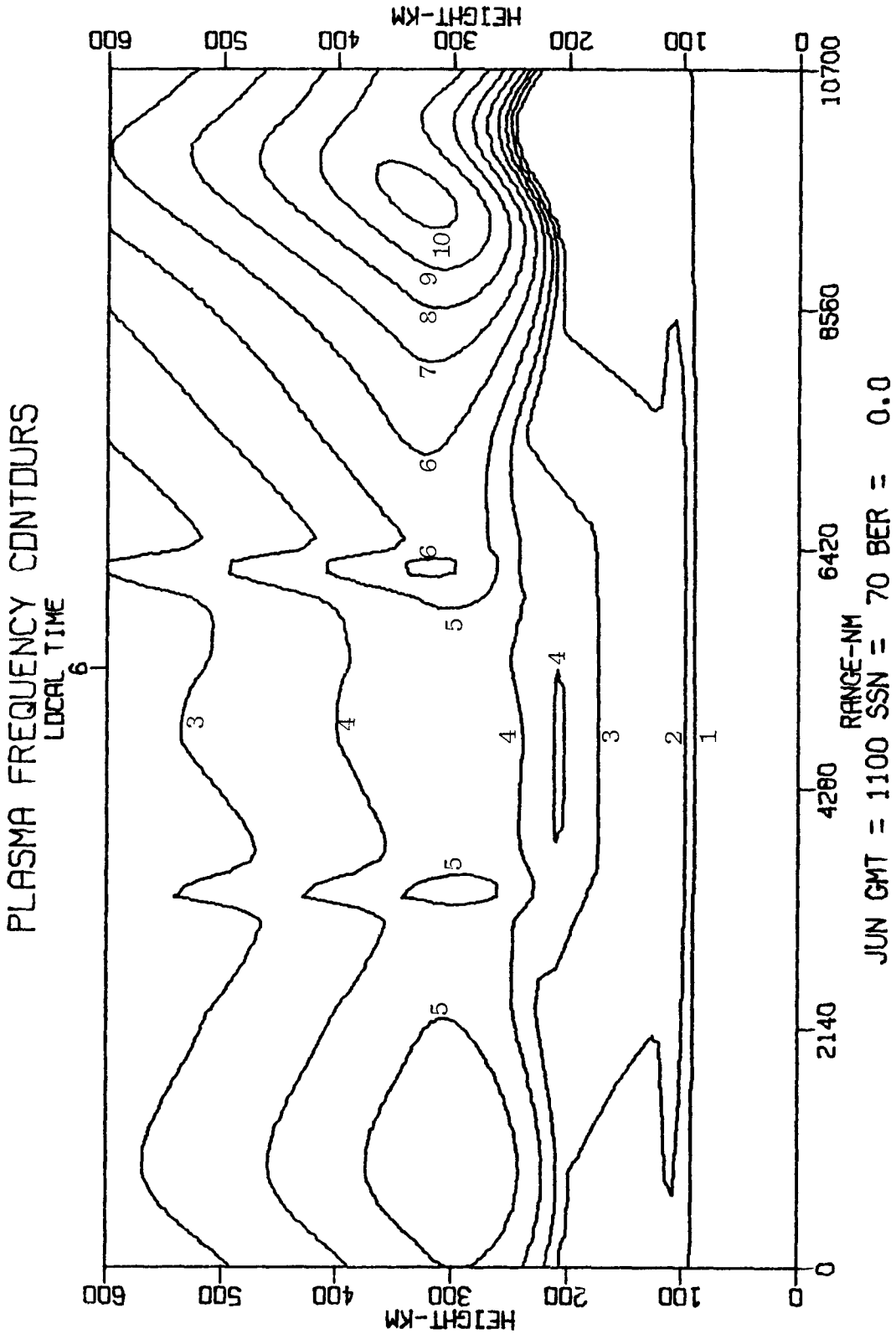


Fig. 19 — June map, 1100 UT, polar corrections ($K_p = 3$)

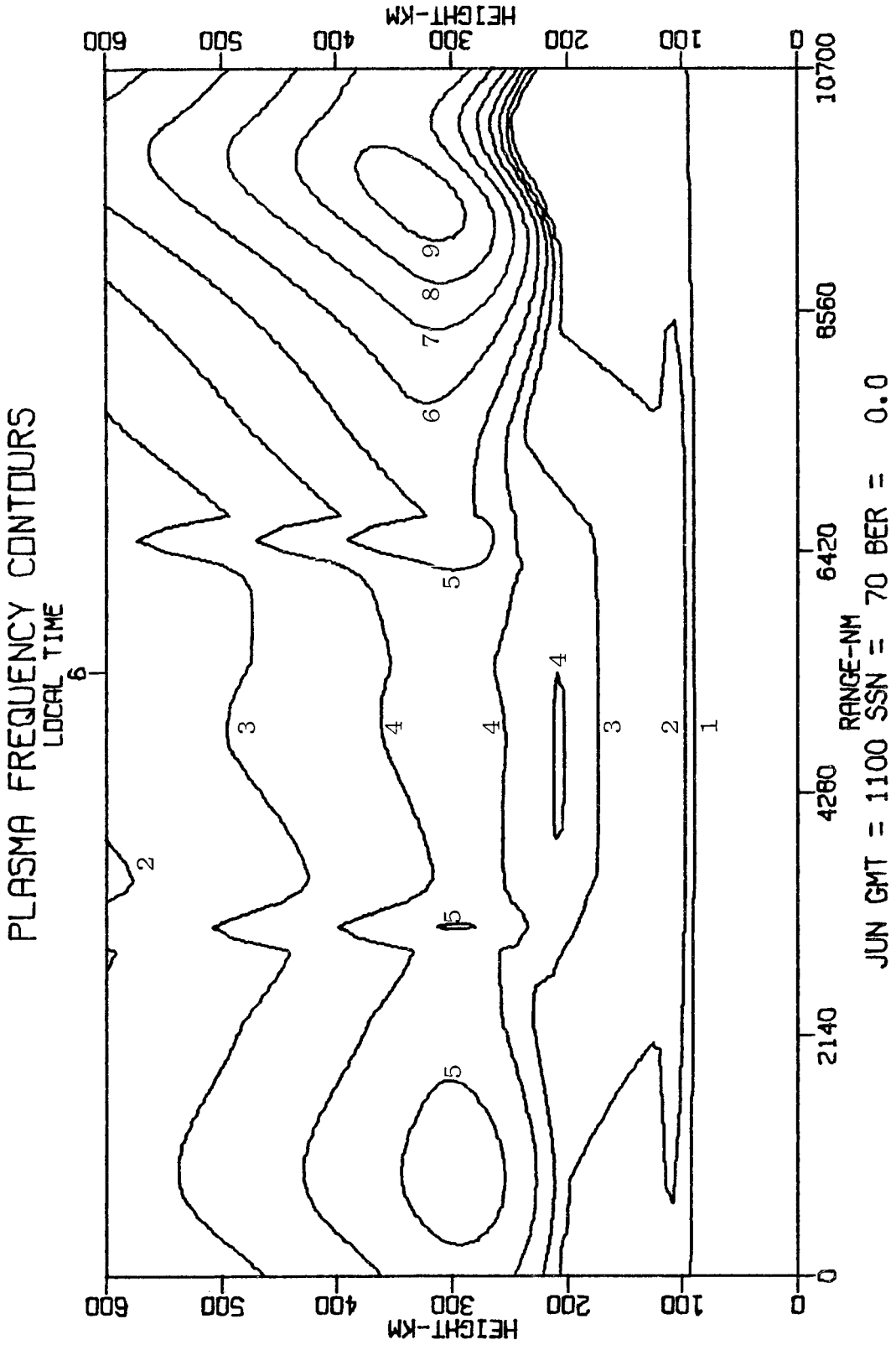


Fig. 20 — June map, 1100 UT, polar corrections ($K_p = 7$)

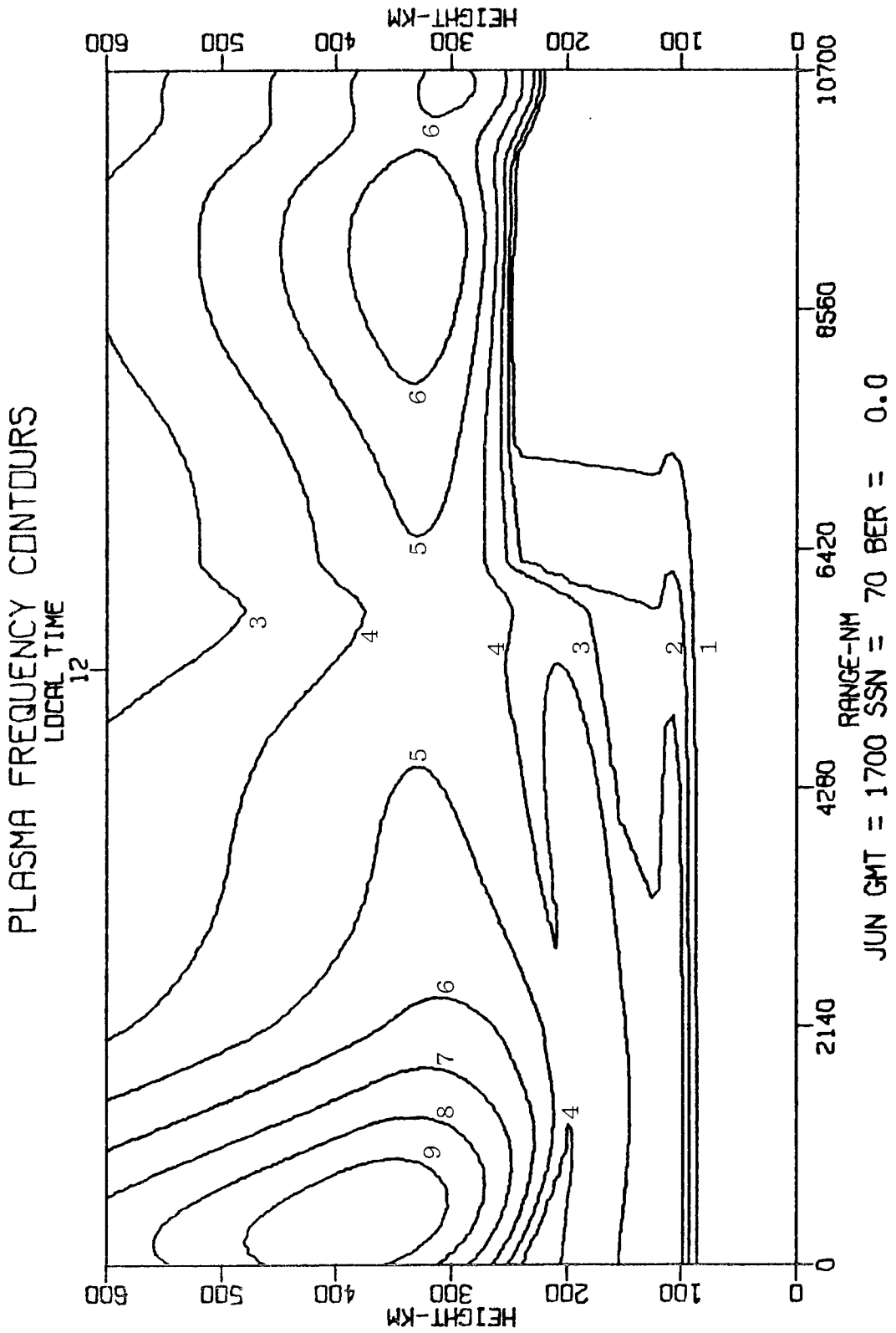


Fig. 21 — June map, 1700 UT, no polar corrections

PLASMA FREQUENCY CONTOURS

LOCAL TIME

12

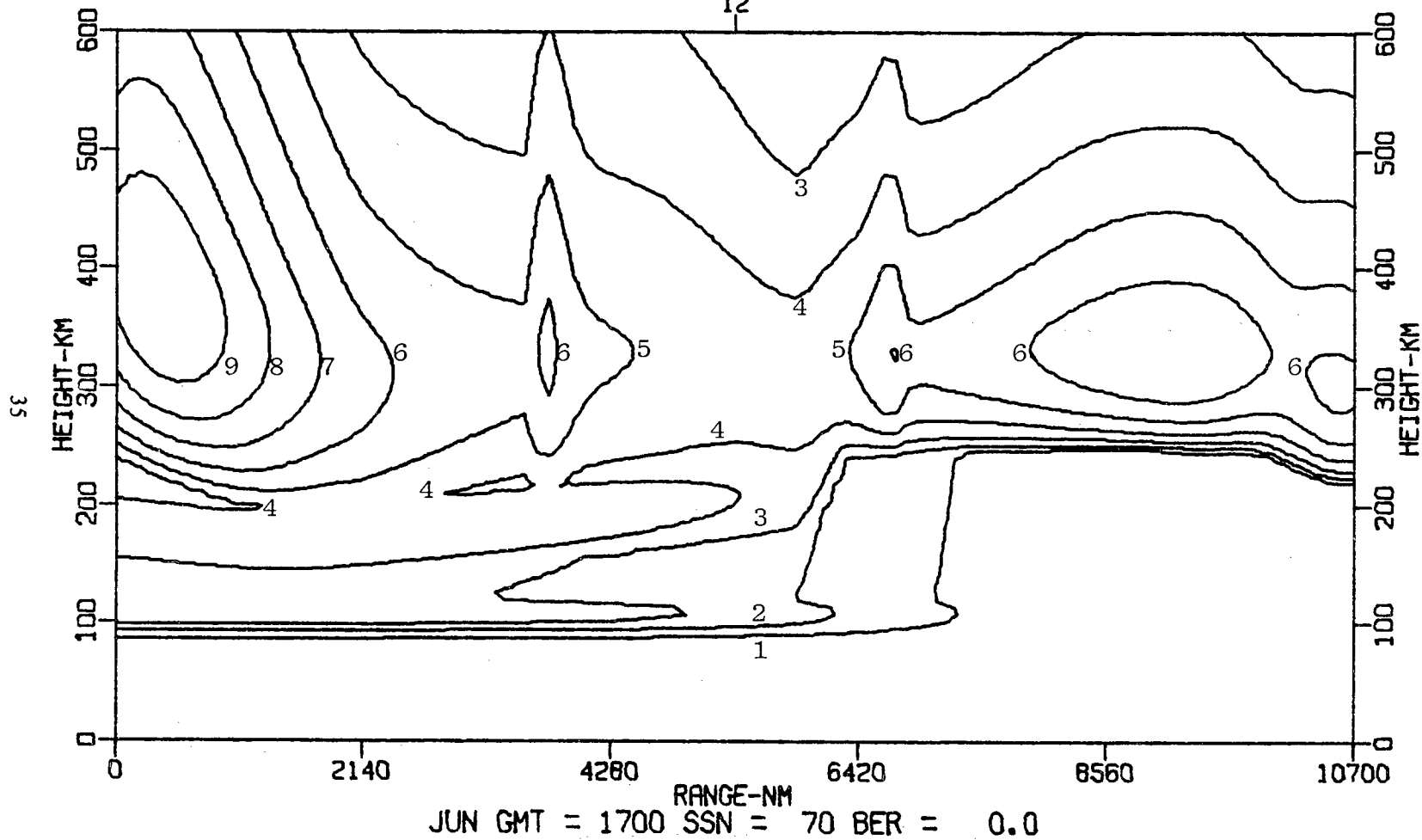


Fig. 22 — June map, 1700 UT, polar corrections ($K_p = 3$)

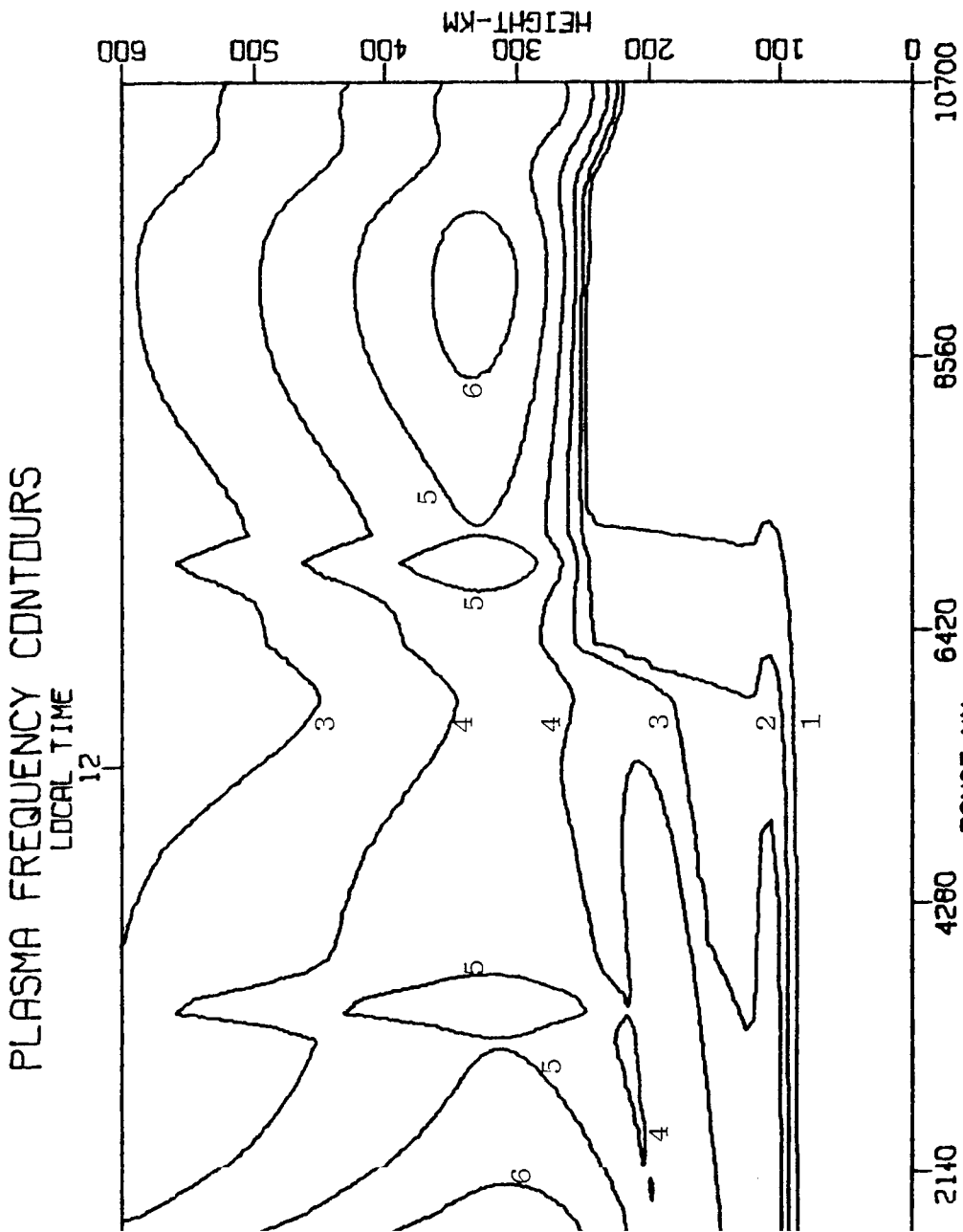


Fig. 23 — June map, 1700 UT, polar corrections ($K_p = 7$)

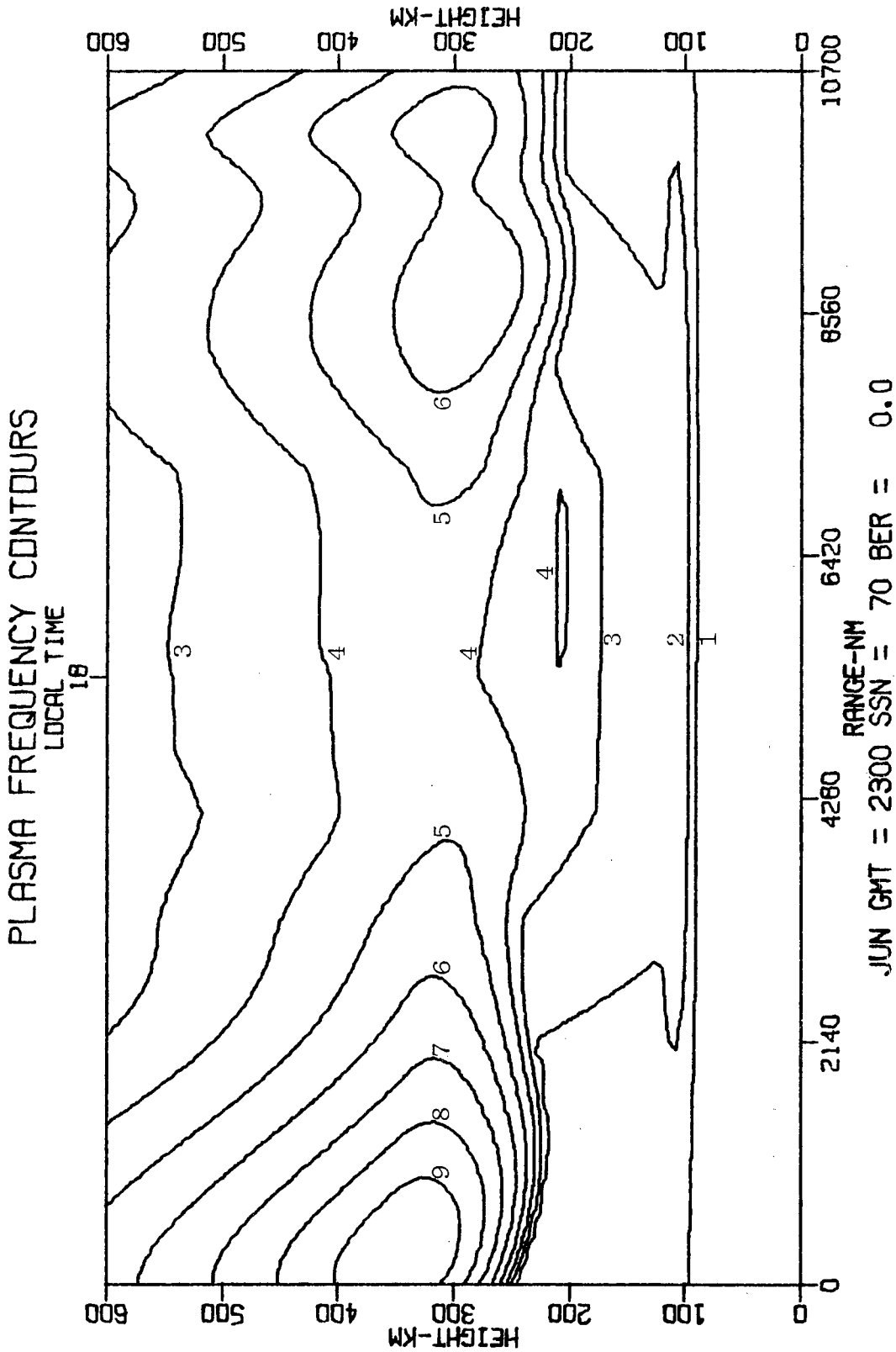


Fig. 24 - June map, 2300 UT, no polar corrections

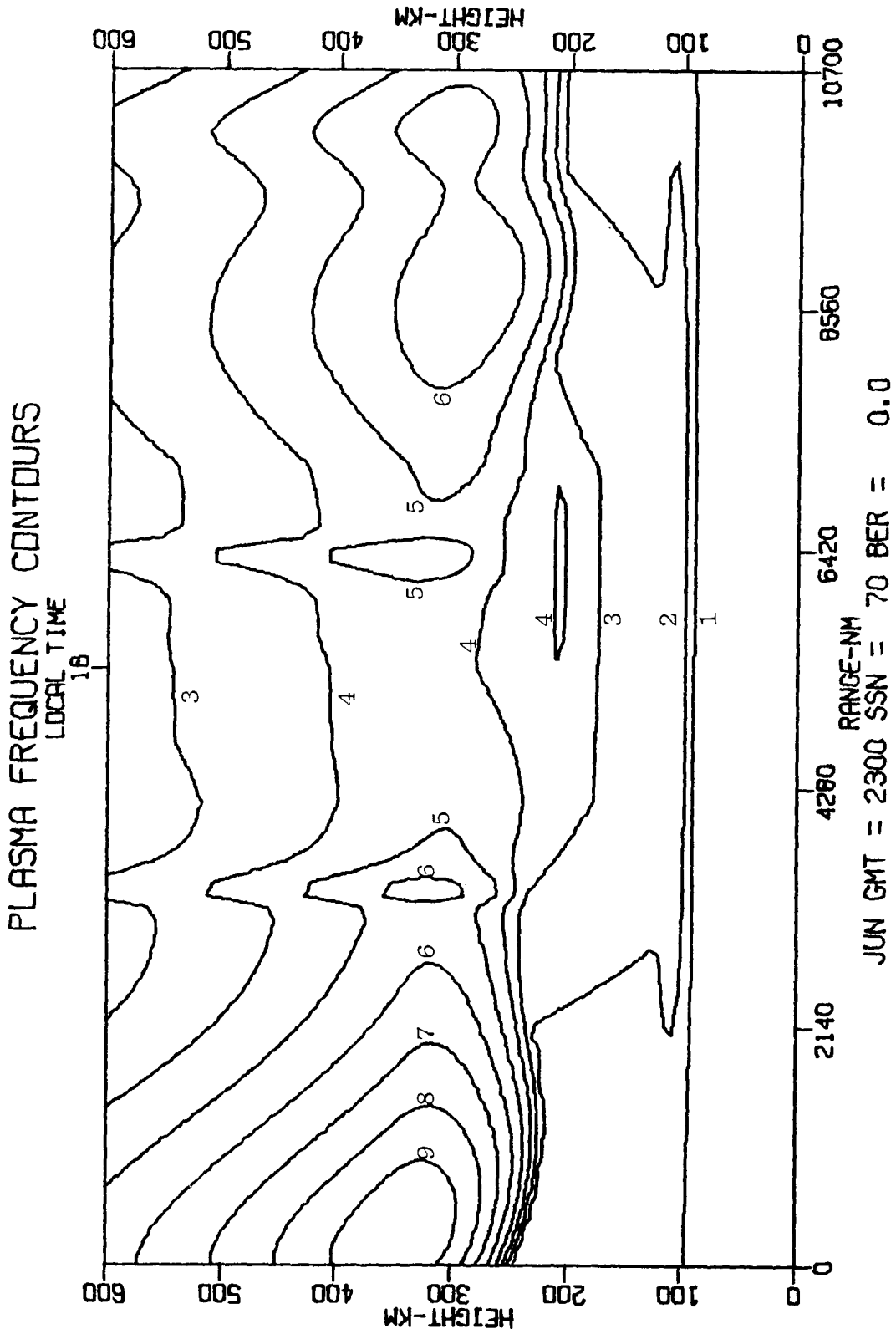


Fig. 25 — June map, 2300 UT, polar corrections ($K_p = 3$)

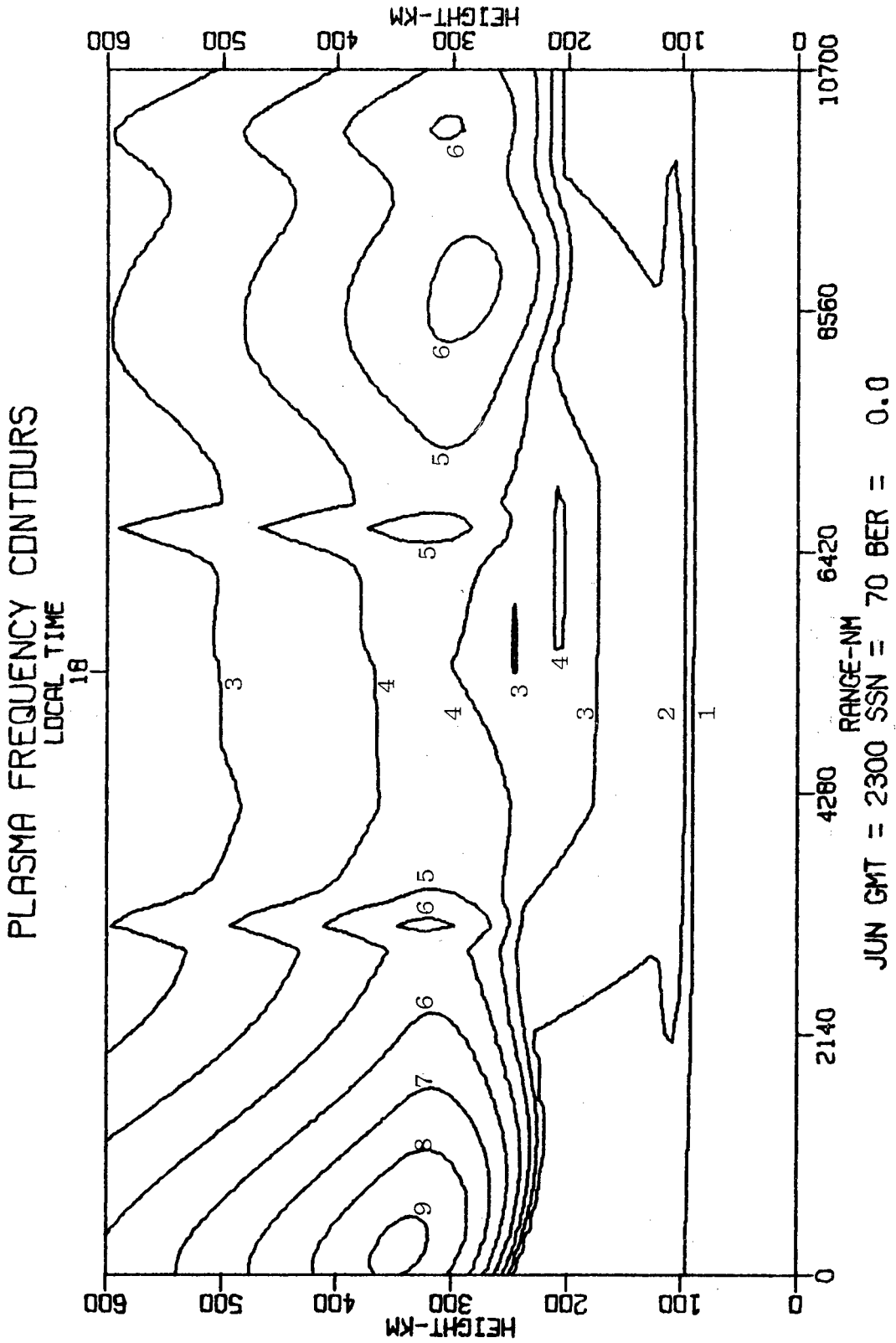


Fig. 26 — June map, 2300 UT, polar corrections ($K_p = 7$)

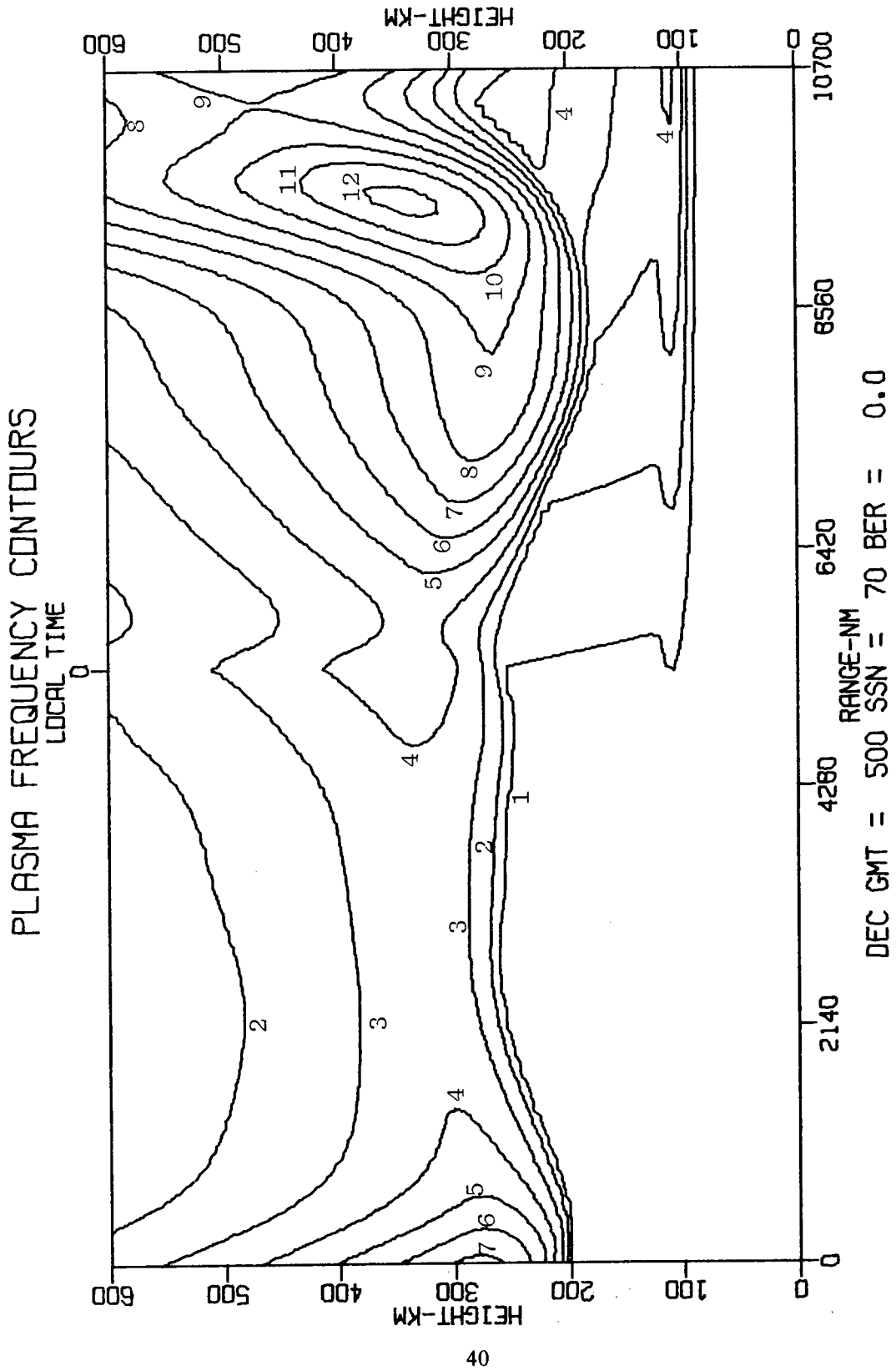


Fig. 27 — December map, 0500 UT, no polar corrections

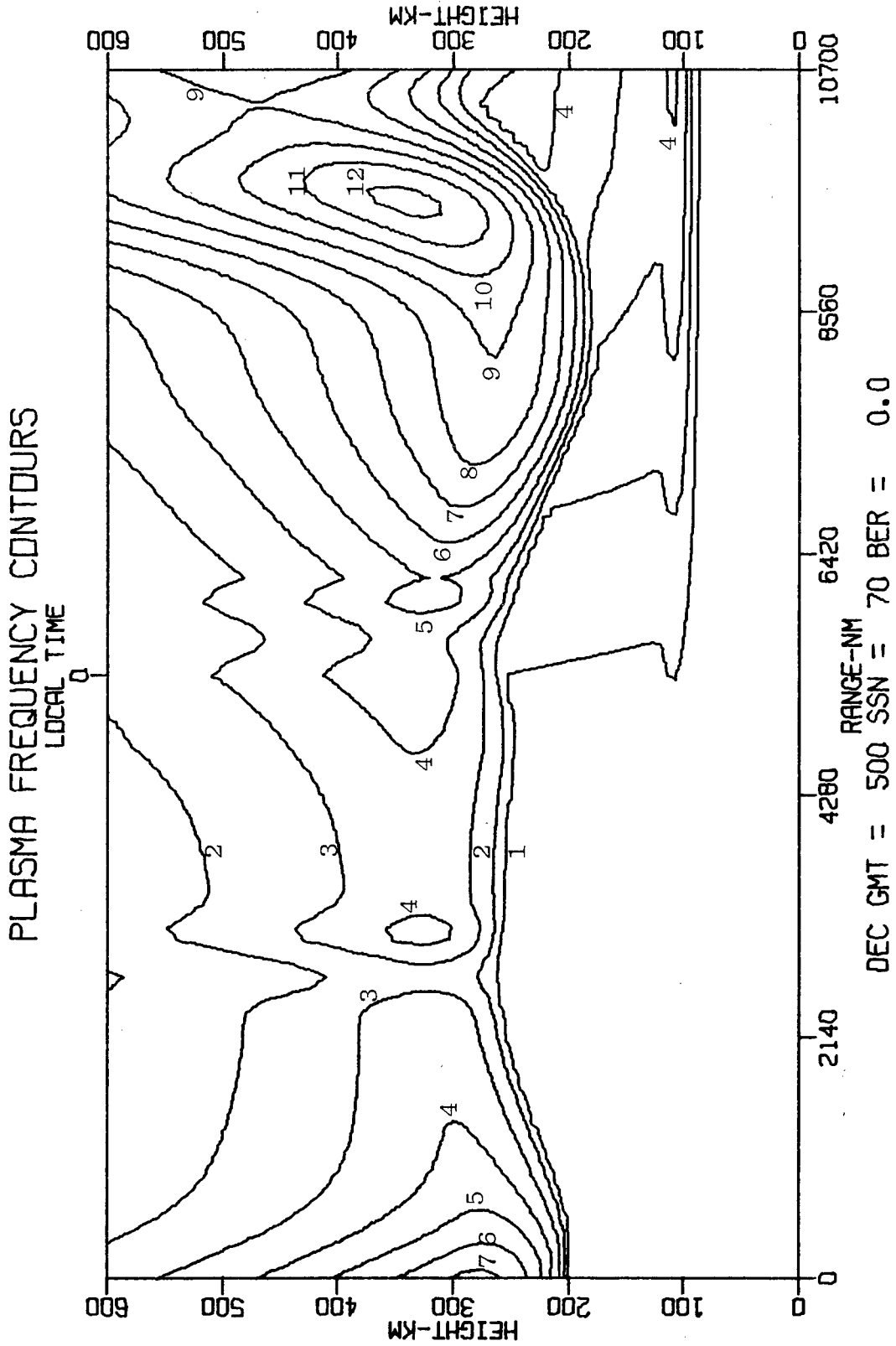


Fig. 28 — December map, 0500 UT, polar corrections ($K_p = 3$)

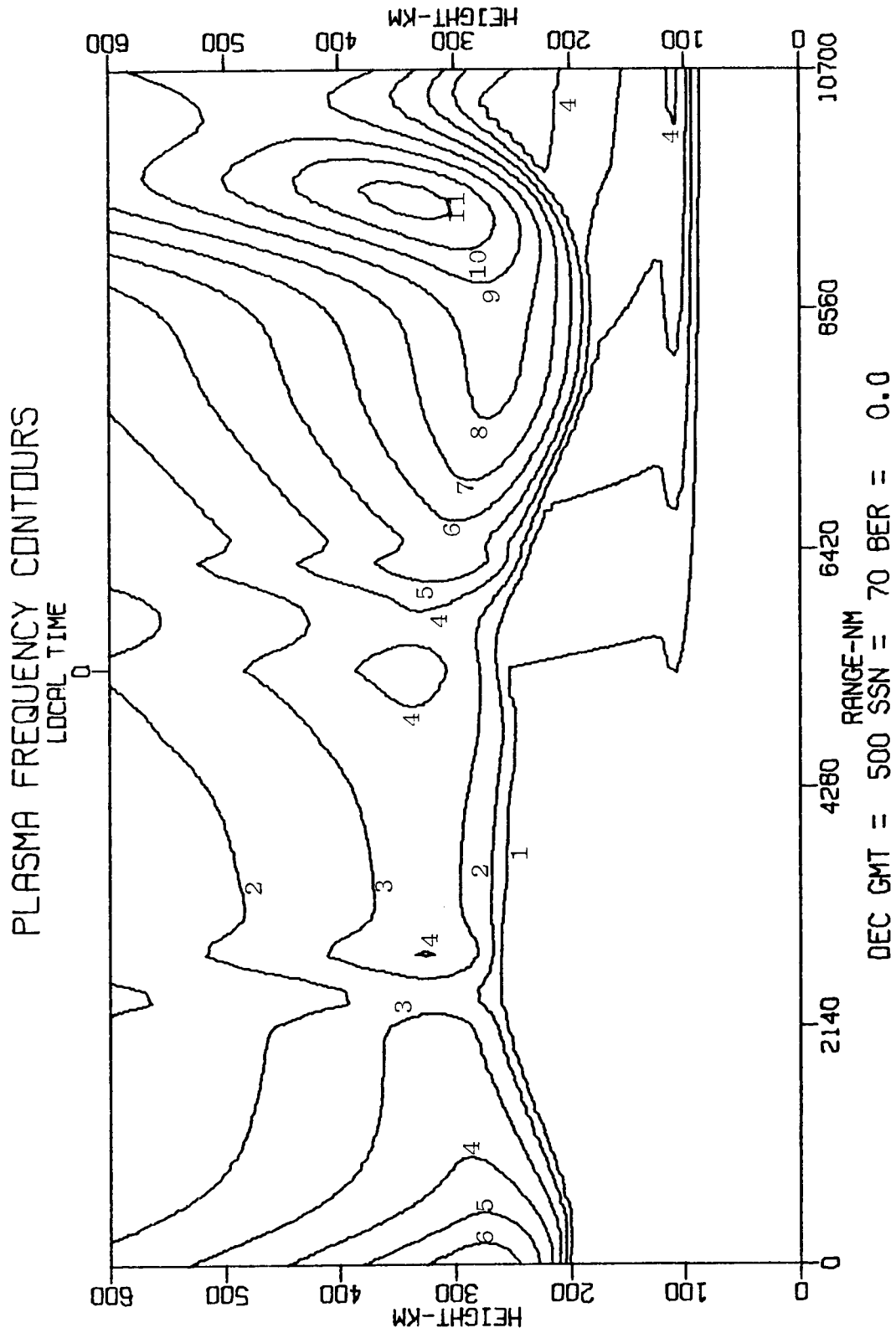


Fig. 29 — December map, 0500 UT, polar corrections ($K_p = 7$)

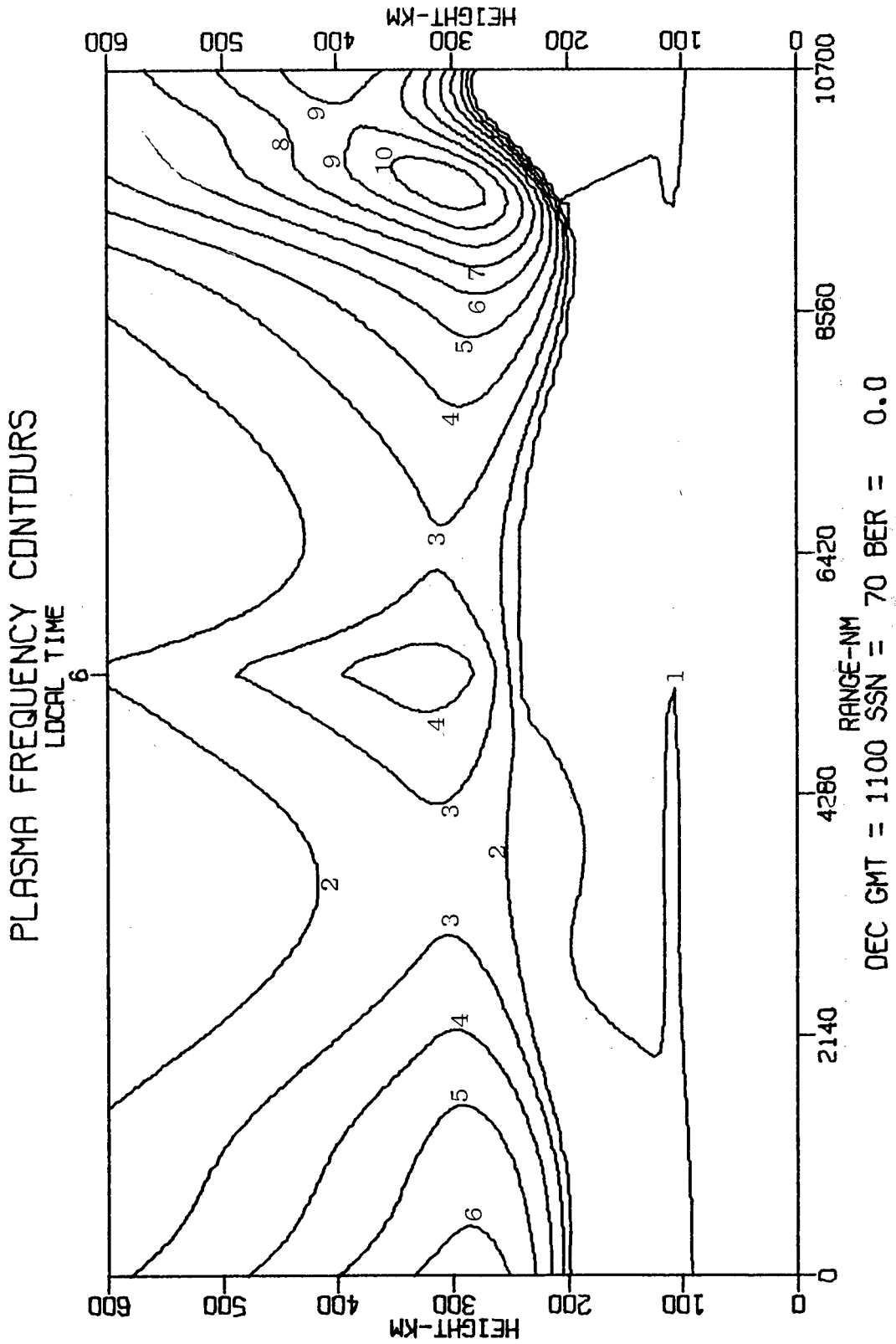


Fig. 30 — December map, 1100 UT, no polar corrections

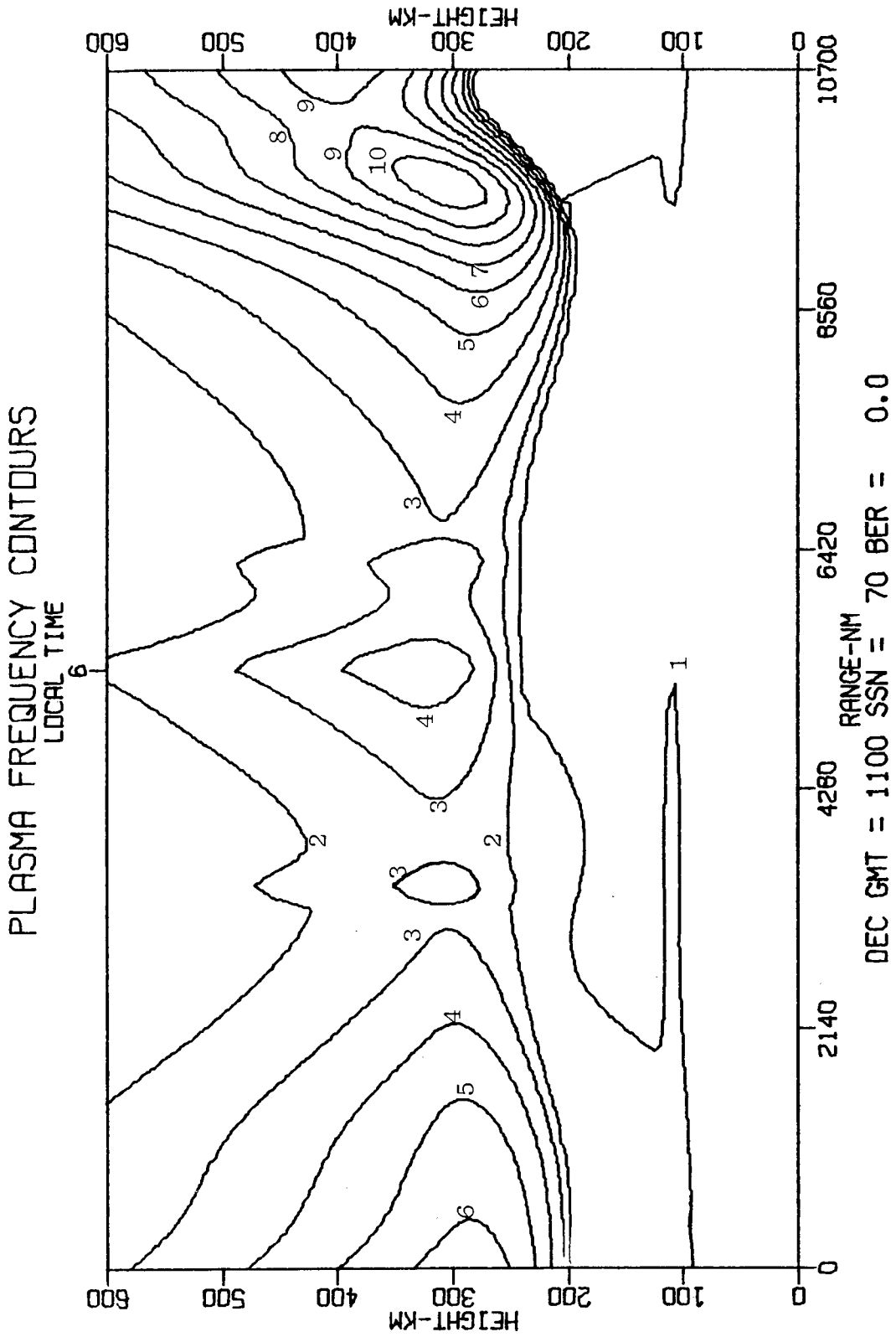


Fig. 31 - December map, 1100 UT, polar corrections ($K_p = 3$)

PLASMA FREQUENCY CONTOURS

LOCAL TIME

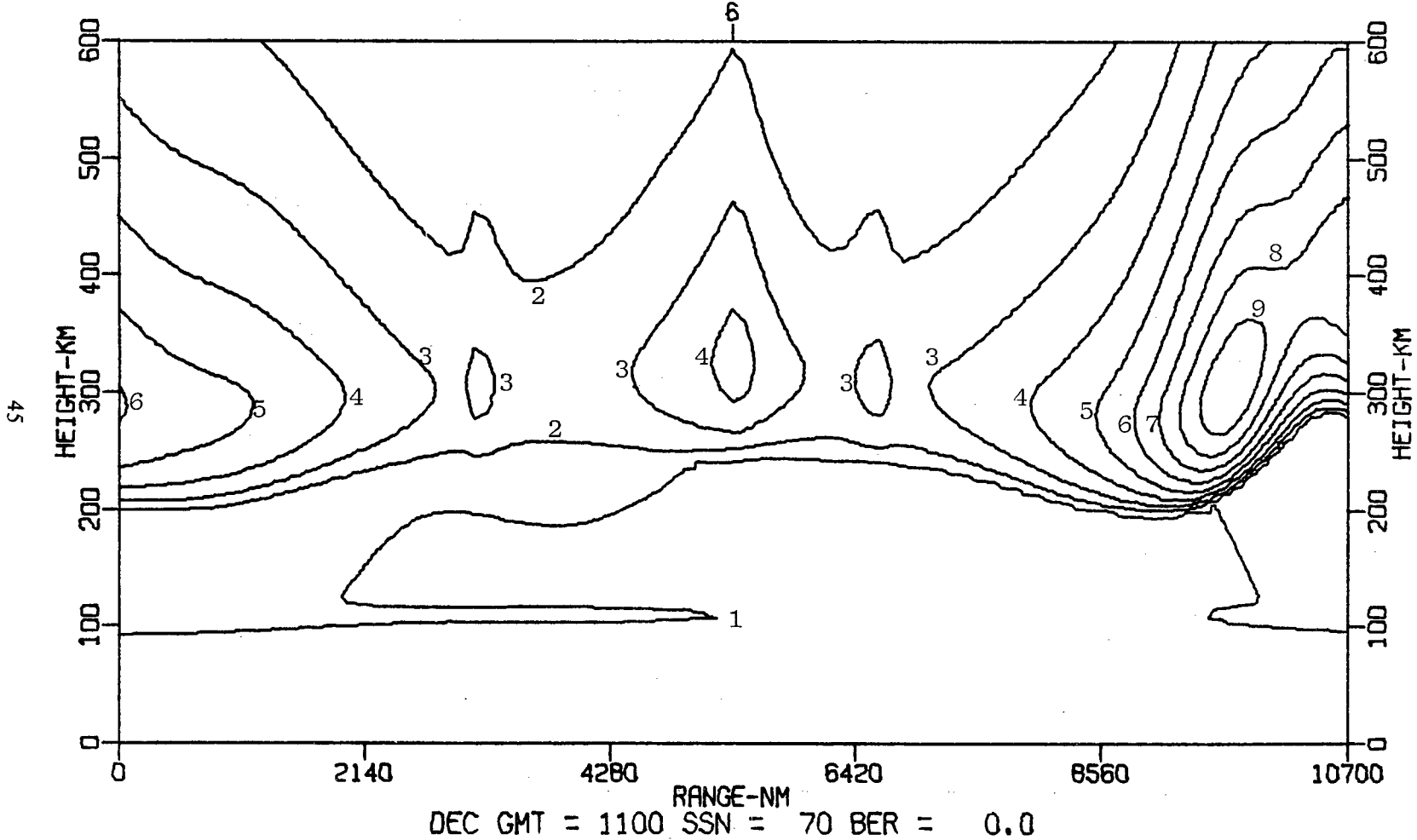


Fig. 32 - December map, 1100 UT, polar corrections ($K_p = 7$)

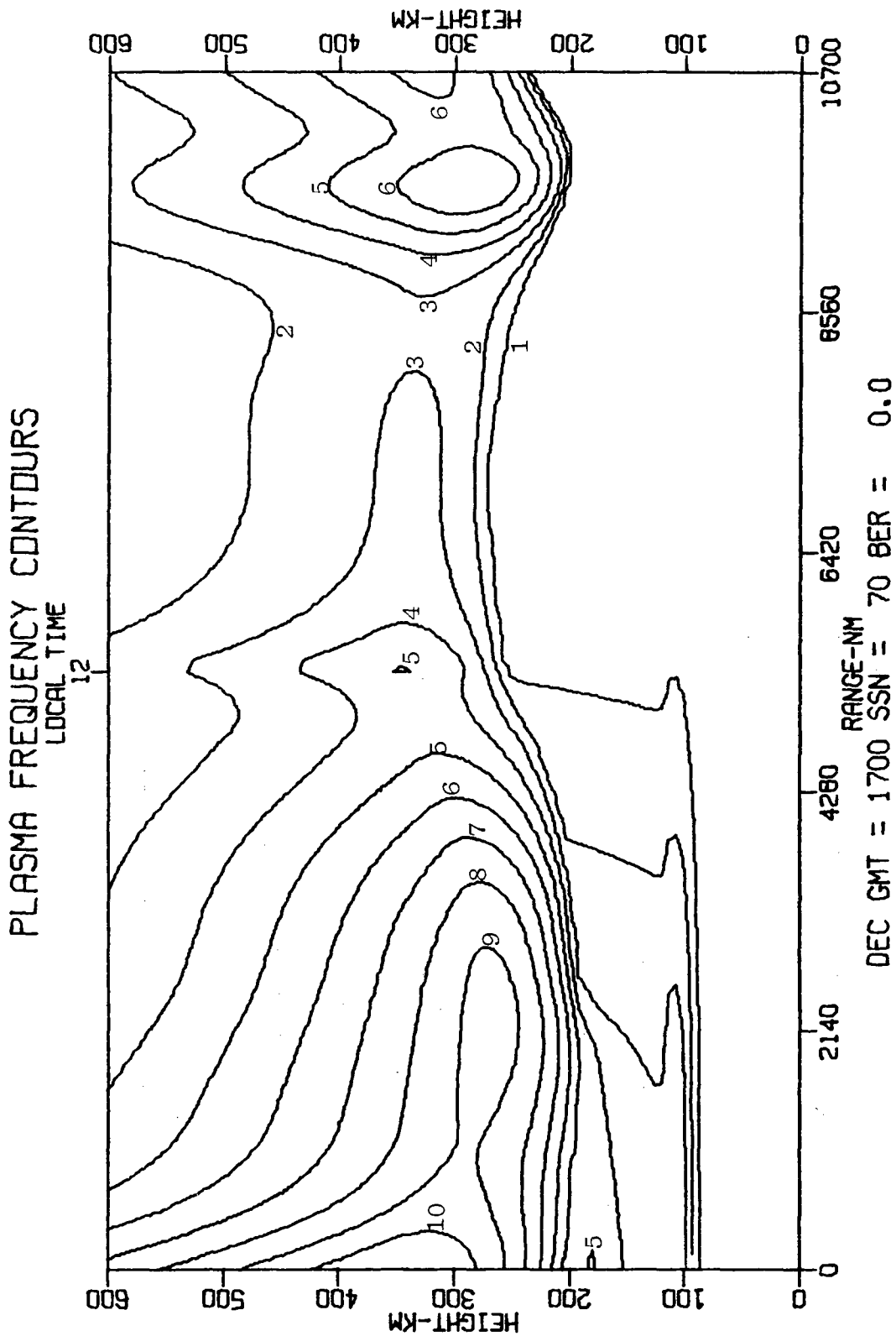


Fig. 33 -- December map, 1700 UT, no polar corrections

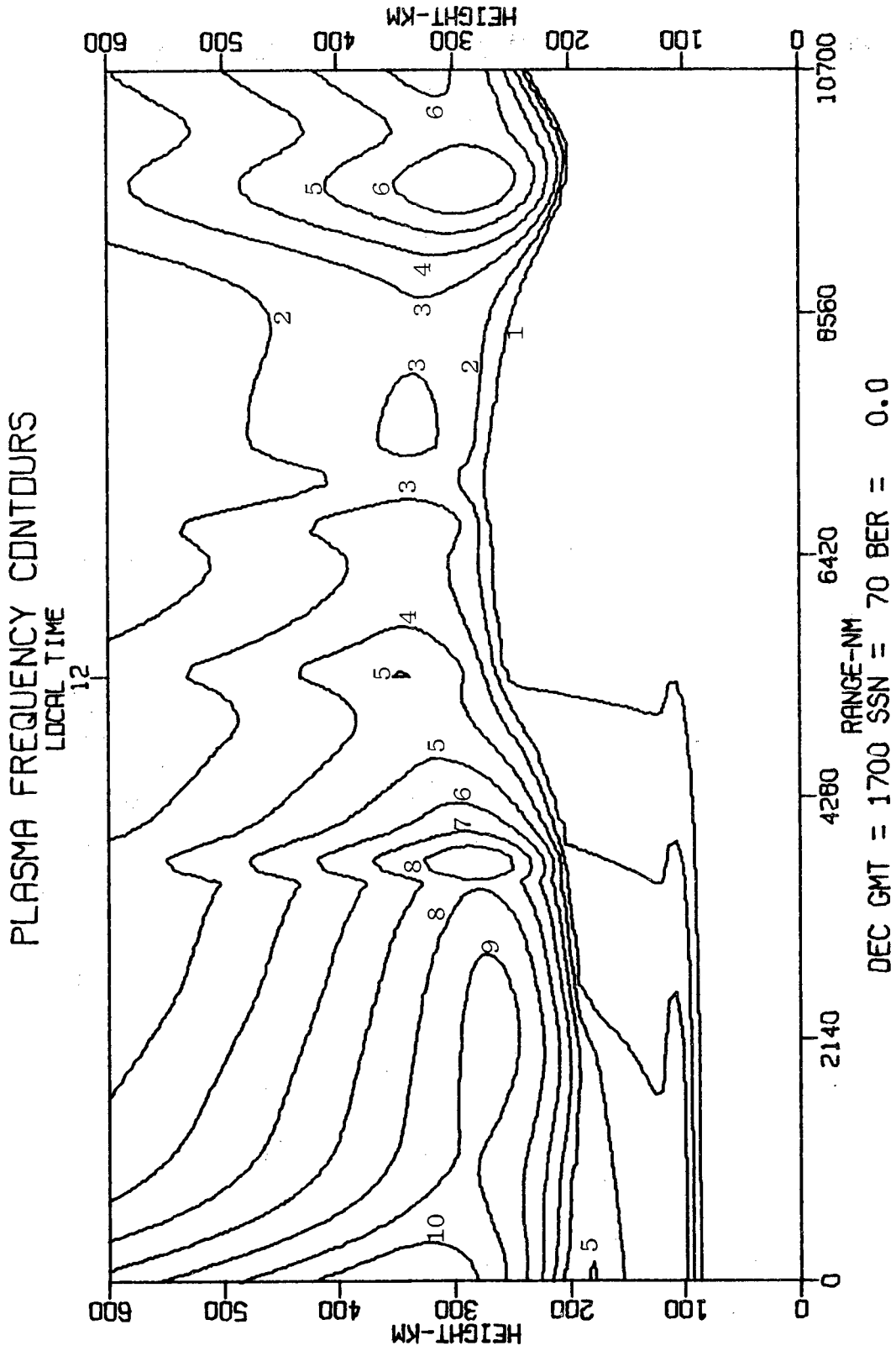


Fig. 34 — December map, 1700 UT, polar corrections ($K_p = 3$)

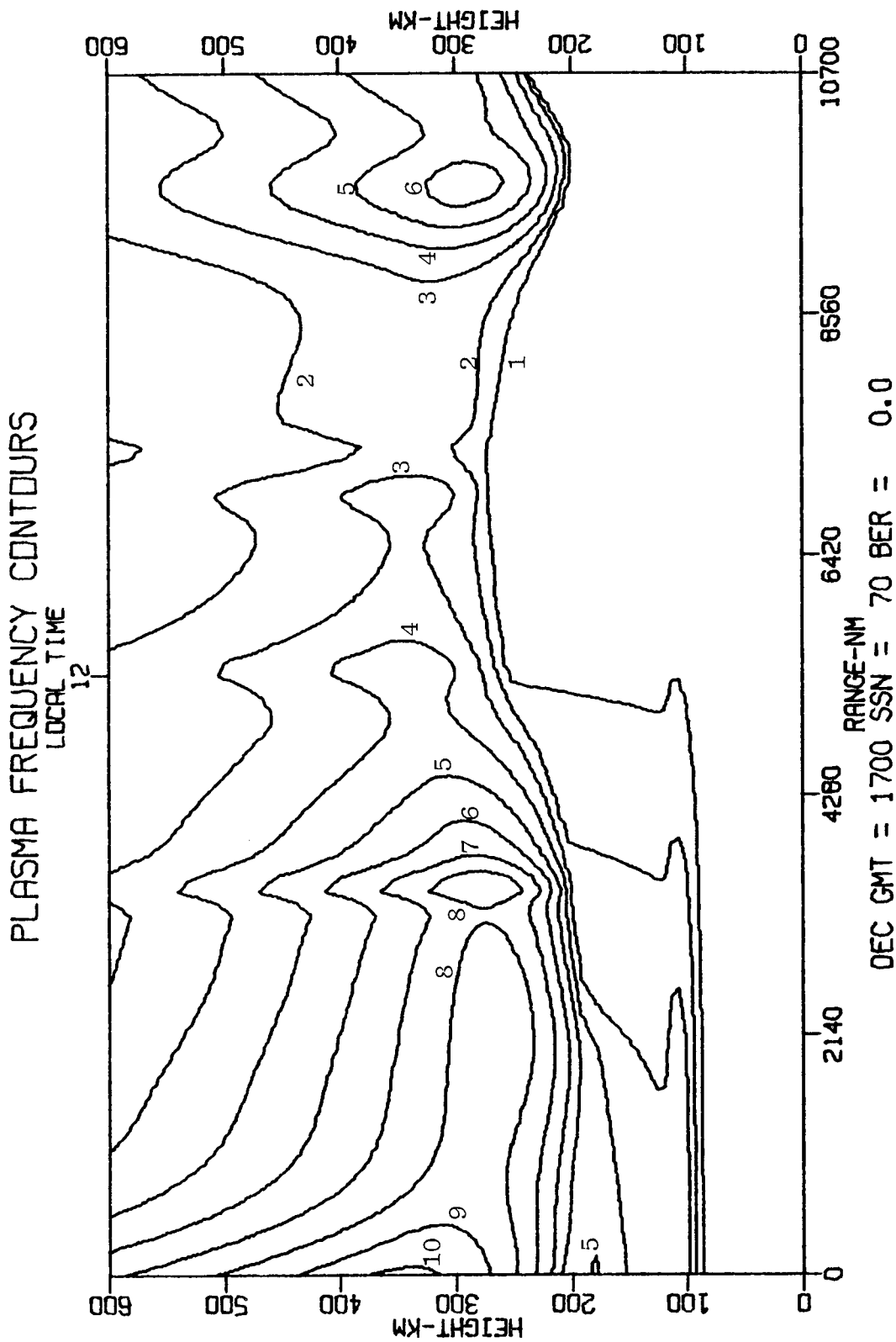


Fig. 35 — December map, 1700 UT, polar corrections ($K_p = 7$)

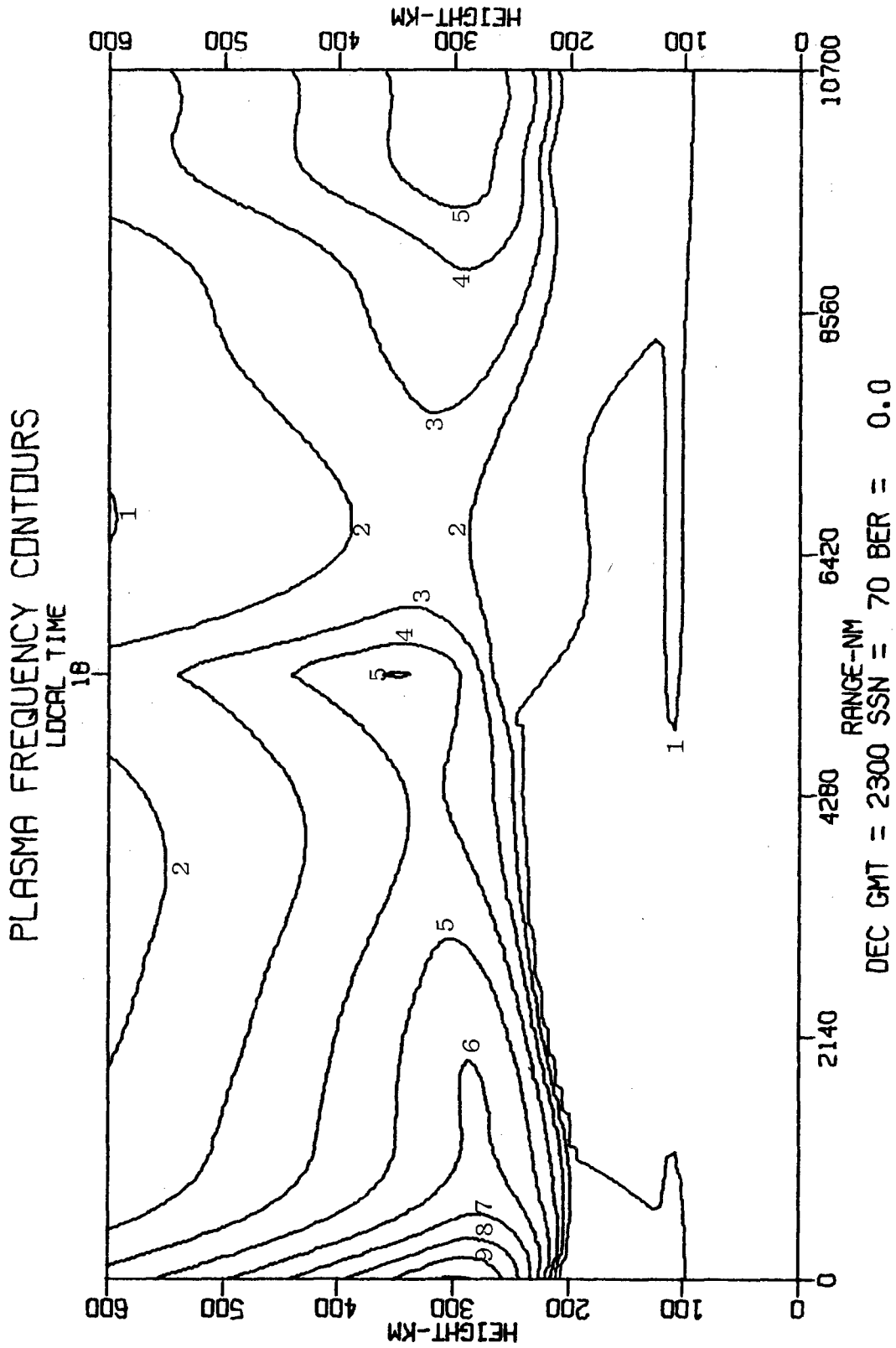


Fig. 36 — December map, 2300 UT, no polar corrections

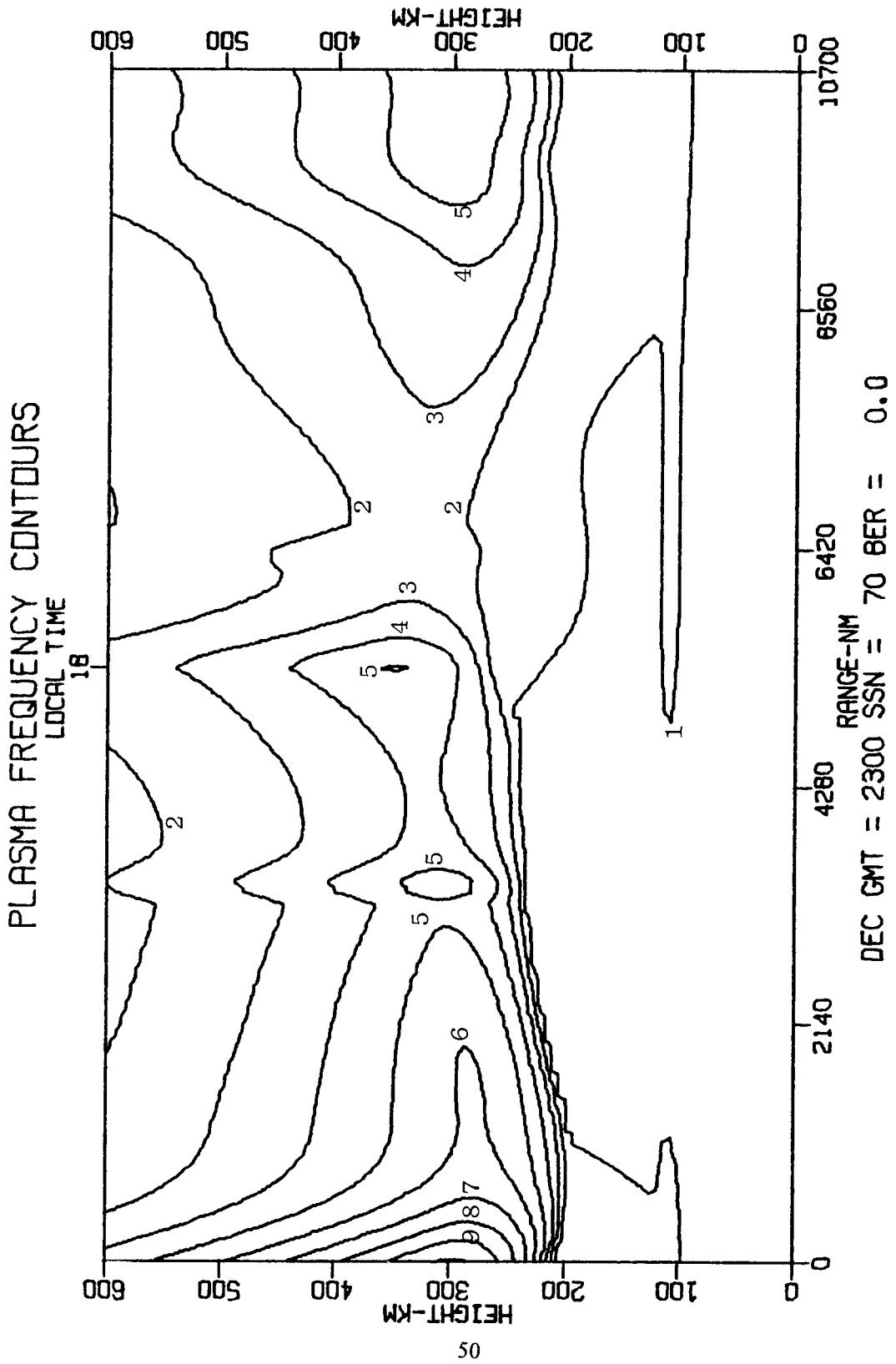
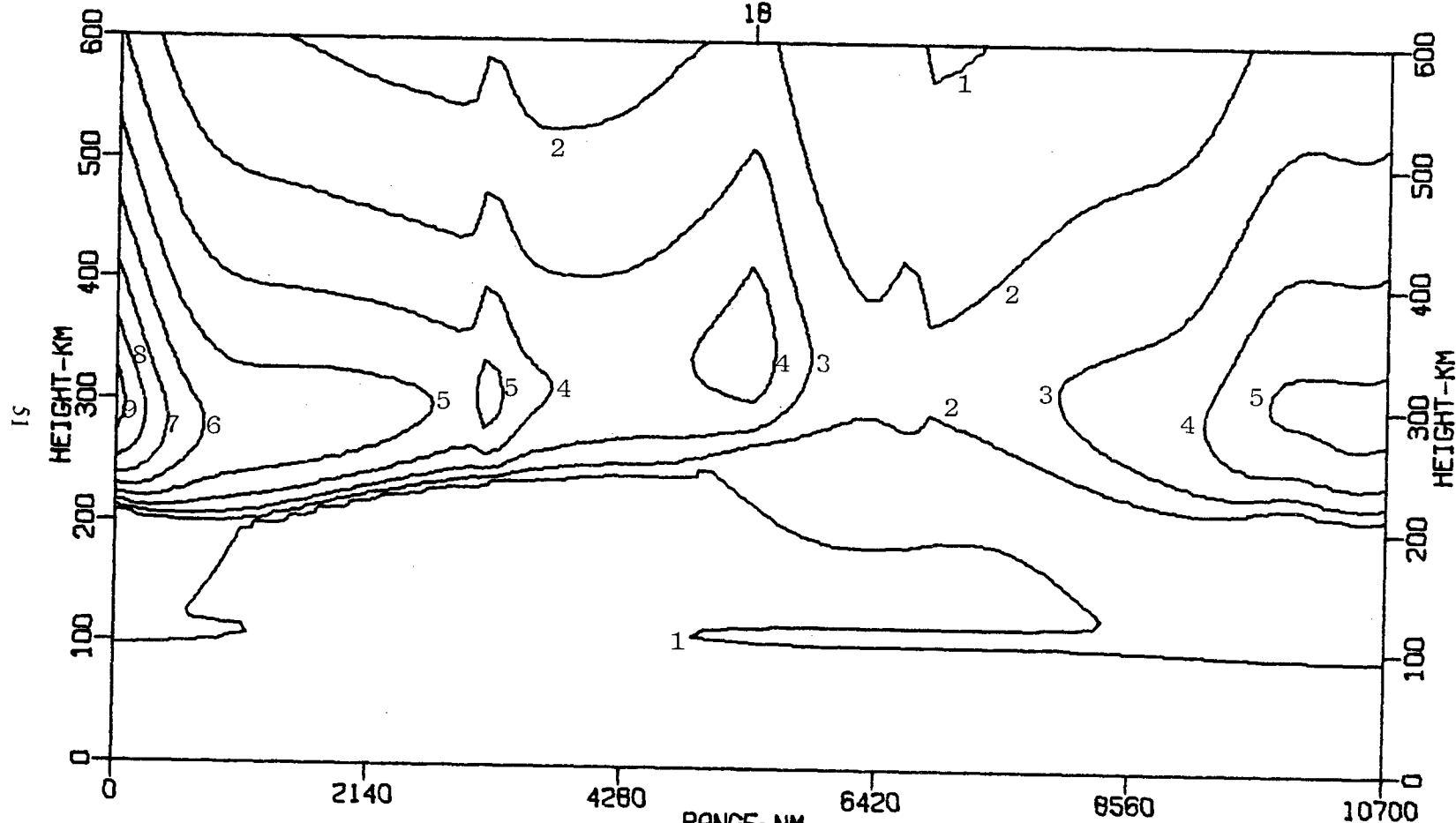


Fig. 37 — December map, 2300 UT, polar corrections ($K_p = 3$)

PLASMA FREQUENCY CONTOURS

LOCAL TIME

18



DEC GMT = 2300 SSN = 70 BER = 0.0

Fig. 38 - December map, 2300 UT, polar corrections ($K_p = 7$)

REFERENCES

1. L. Kelley, "Calculation of Sky-Wave Field Intensities, Maximum Usable Frequencies," U.S. Army Signal Corps Tech. Rept. No. 6, (1945).
2. Central Radio Propagation Laboratory, "Ionospheric Radio Propagation," NBS Circular 462 (June 1948).
3. P.O. Laitinen and G.W. Haydon, "Analysis and Prediction of Sky-Wave Field Intensities in the High Frequency Band," U.S. Army Signal Radio Propagation Agency Tech. Rept. No. 9 (AD 291 505) (Oct. 1962).
4. Stanford Research Institute, "The Application of Digital Computing Techniques to the Problem of Interference on HF Communication Circuits and Networks," Spec. Rept. 1, SRI Project 2124 (AD 310 180) (Dec. 1957).
5. D.L. Lucas and G.W. Haydon, "MUF-FOT Predictions by Electronic Computers" NBS Rept. 6789 (Aug. 1961).
6. W.B. Jones and R.M. Gallet, "The Representation of Diurnal and Geographic Variations of Ionospheric Data by Numerical Methods," NBS Journal **66D**(4): 419-438 (July-Aug. 1962).
7. D.L. Lucas and G.W. Haydon, "Predicting the Performance of Band 7 Communications Systems Using Electronic Computers," NBS Rept. 7619 (AD 266 585) (1962).
8. D.L. Lucas and G.W. Haydon, "Predicting Statistical Performance Indexes for High Frequency Telecommunications Systems," ESSA Tech. Rept. IER-ITSA 1 (AD 644 827) (Aug. 1966).
9. A.F. Barghausen, J. Finney, L. Proctor, and L. Schultz, "Predicting Long-Term Operational Parameters of High-Frequency Sky-Wave Telecommunication Systems," ESSA Tech. Rept. ERL 110-ITS 78 (May 1969).
10. J.M. Headrick, J. Thomason, D. Lucas, S. McCammon, R. Hanson, and J. Lloyd, "Virtual Path Tracing for HF Radar Including an Ionospheric Model," NRL Memo Rept. 2226 (AD 883 463L) Mar. 1971.
11. D. Lucas, J. Lloyd, J.M. Headrick and J. Thomason, "Computer Techniques for Planning and Management of OTH Radar," NRL Memo Rept. 2500 (AD 748 588) Sept. 1972.
12. M. Leftin, "Numerical Representation of Monthly Median Critical Frequencies of the Regular E Region (f_oE)," Office of Telecommunications Rept. 76-88 (1976).
13. M. Leftin, S. Ostrow, and C. Preston, "Numerical Maps of f_oE_s for Solar Cycle Minimum and Maximum," ESSA Tech. Rept. ERL 73-ITS 63 (1968).
14. W. R. Piggot and K. Rawer, *URSI Handbook of Ionogram Interpretation and Reduction*, Elsevier Publishing Co., New York, N.Y., 1961.

15. C.C.I.R., "Atlas of Ionospheric Characteristics," International Telecommunication Union Rept. 340, Oslo (1966).
16. T. Shimazaki, "World-Wide Daily Variations in the Height of the Maximum Electron Density of the Ionospheric F2 Layer," J. Radio Res. Labs., Japan, 2(7): 85-97 (Jan. 1955).
17. R.K. Rosich and W.B. Jones, "The Numerical Representation of the Critical Frequency of the F_1 Region of the Ionosphere," Office of Telecommunications Rept. 73-22 (COM-75-10813) (Oct. 1973).
18. K. Rawer, *Meteorological and Astronomical Influences on Radio Wave Propagation*, p. 221-250, Pergamon Press, 1963.
19. David C. Miller and Joseph Gibbs, "Ionospheric Analysis and Ionospheric Modeling," AFCRL Tech. Rept. 75-0549 (AD A020-272) (July 1975).
20. G. Gustafsson, "A Revised Corrected Geomagnetic Coordinate System," Arkiv Foer Geofysik, Band 5, nr 40 (1970).
21. G. Nestorov, "Exponential Model of the Ionospheric D-Region," Geomagn. Aeron., 12 (1) 36-44 (1972).
22. R.B. Bent, S. Llewellyn, G. Nesterczuk, and P. Schmid, "The Development of a Highly Successful Worldwide Empirical Ionospheric Model and Its Use in Certain Aspects of Space Communications and Worldwide Total Electron Content Investigations," NRL Symposium Proceedings (AD-A023 510) (1975).
23. R.M. Jones and J.J. Stephenson, "A Versatile Three-Dimensional Ray Tracing Computer Program for Radio Waves in the Ionosphere," Office of Telecommunication Rept. 75-76 (PB248856) (Oct. 1975).
24. M. Friedman, D. Miller, K. Vangri, J. Gibbs, J. Hsiung, J. Tardelli, E. Cohen, and J. O'Brien, "Mathematical and Statistical Analysis for the Reduction of Ionospheric Data and Other Physical Systems," AFCRL Tech. Rept. 73-0049 (AD 757 480) (Nov. 1972).

